

1 **Field assessments on impact of CO<sub>2</sub> concentration fluctuations along with complex**  
2 **terrain flows on the estimation of the net ecosystem exchange of temperate forests**

3 Dexiong Teng<sup>1,2</sup>, Jiaojun Zhu<sup>1,2,3,\*</sup>, Tian Gao<sup>1,2,3</sup>, Fengyuan Yu<sup>1,2</sup>, Yuan Zhu<sup>1,2</sup>, Xinhua  
4 Zhou<sup>3,4</sup>, Bai Yang<sup>4</sup>

5 1 CAS Key Laboratory of Forest Ecology and Silviculture, Institute of Applied Ecology, Chinese  
6 Academy of Sciences, Shenyang 110000, China

7 2 Qingyuan Forest CERN, National Observation and Research Station, Liaoning Province,  
8 Shenyang 110016, China

9 3 CAS-CSI Joint Laboratory of Research and Development for Monitoring Forest Fluxes of Trace  
10 Gases and Isotope Elements, Institute of Applied Ecology, Chinese Academy of Sciences,  
11 Shenyang 110016, China

12 4 Campbell Scientific Incorporation, Logan, Utah 84321, USA

13 **\* Corresponding Author: Jiaojun Zhu**

14 Tel : +86 24 83970342

15 Email: [jiaojunzhu@iae.ac.cn](mailto:jiaojunzhu@iae.ac.cn)

16 **Abstract**

17       The CO<sub>2</sub> storage ( $F_s$ ) is the cumulation or depletion in CO<sub>2</sub> amount over a period  
18 in an ecosystem. Along with the eddy-covariance flux and wind-stream advection of  
19 CO<sub>2</sub>, it is a major term in the net ecosystem CO<sub>2</sub> exchange (NEE) equation and even  
20 dominates in the equation under a stable atmospheric stratification while this equation  
21 is used for forest ecosystems over complex terrains. However, estimating the  $F_s$  remains  
22 challenging due to the frequent gusts and random fluctuations in boundary-layer flows  
23 that arouse tremendous difficulties in catching the true trend of CO<sub>2</sub> changes for its  
24 storage estimation from eddy-covariance along with the atmospheric profile techniques.  
25 Using the measurements from Qingyuan Ker Towers equipped with NEE instrument  
26 systems separately covering mixed-broadleaf, oak, and larch forests towers in a  
27 mountain watershed, this study investigates the gust periods and CO<sub>2</sub> fluctuation  
28 magnitudes while examining their impact on  $F_s$  estimation in relation to the terrain  
29 complexity index (TCI). The gusts induce CO<sub>2</sub> fluctuations at numerous periods of 1 to  
30 10 min over two hours. Diurnal, seasonal, and spatial differences ( $P < 0.01$ ) in the  
31 maximum amplitude of CO<sub>2</sub> fluctuations ( $A_m$ ) ranges from 1.6 to 136.7 ppm and these  
32 difference in a period ( $P_m$ ) at the same significant level ranges 140 to 170 second. The  
33  $A_m$  and  $P_m$  are significantly correlated to the magnitude and random error of  $F_s$  with  
34 diurnal and seasonal differences. These correlations decrease as CO<sub>2</sub> averaging time  
35 windows becomes longer. To minimize the uncertainties of  $F_s$ , a constant [CO<sub>2</sub>]  
36 averaging time window for the  $F_s$  estimates is not ideal. Dynamic averaging time  
37 windows and a decision-level fusion model can reduce the potential underestimation of

38  $F_s$  by 29%–33%, being equivalent to 1.9%–4.3% underestimation of the NEE for  
 39 temperate forests in complex terrains. The relative contribution of  $F_s$  to the 30-min NEE  
 40 observations ranged from 17% to 82% depending on turbulent mixing and TCI. The  
 41 study's approach is notable as it incorporates TCI and utilizes three flux towers for  
 42 replication, making the findings relevant to similar regions with a single tower.

43 **Keywords:** Eddy covariance, complex terrain, carbon flux, storage term, carbon  
 44 dioxide concentration, random uncertainty

## 45 **1 Introduction**

46 The accurate estimation of the net ecosystem exchange (NEE) of carbon dioxide  
 47 ( $\text{CO}_2$ ) in forest ecosystems is crucial for a comprehensive understanding of the global  
 48 carbon cycle. The eddy covariance (EC) technique has been widely used in forest  
 49 ecosystems due to its capacity to directly measure the NEE while measurement  
 50 conditions satisfy the underlying theory. The EC technique is based on a simplified  
 51 mass conservation equation (after the Reynolds averaging), given by:

$$\begin{aligned}
 \text{NEE} = & \underbrace{\frac{1}{V_m} \int_0^h \left( \frac{\partial \bar{c}}{\partial t} \right) dz}_{\text{I}} + \underbrace{\frac{1}{V_m} (\overline{w'c'})}_h}_{\text{II}} \\
 & + \underbrace{\frac{1}{V_m} \int_0^h \left( \bar{w}(z) \frac{\partial \bar{c}}{\partial z} \right)}_{\text{III a}} + \underbrace{\bar{c}(z) \frac{\partial \bar{w}}{\partial z}}_{\text{III b}} dz, \quad (1) \\
 & + \underbrace{\frac{1}{V_m} \int_0^h \left( \bar{u}(z) \frac{\partial \bar{c}}{\partial x} + \bar{v}(z) \frac{\partial \bar{c}}{\partial y} \right)}_{\text{IV}} dz
 \end{aligned}$$

53 where  $V_m$  is the volume of dry air in the control volume;  $c$  is the  $\text{CO}_2$  mixing ratio;  $t$  is  
 54 the time;  $h$  is the measure height;  $u$ ,  $v$ , and  $w$  denote the velocity components in the  $x$ ,

55  $y$ , and  $z$  directions, respectively; and an overbar denotes Reynolds averaging. This  
56 equation conceptualizes the NEE within a control volume from the ground to the  
57 measurement height ( $h$ ), while ignoring the horizontal turbulence term divergence  
58 (Feigenwinter et al., 2004). In this equation, term I is the CO<sub>2</sub> storage ( $F_s$ ) representing  
59 the change in the average CO<sub>2</sub> concentration (hereafter [CO<sub>2</sub>]). Terms II, IIIa, IIIb, and  
60 IV represent the vertical turbulent flux ( $F_c$ ), the vertical advection, the interface vertical  
61 mass advection, such as the evaporation process (Webb et al., 1980), and the horizontal  
62 advection, respectively.

63 Most flux measurements typically lack the solutions for terms III and IV, and can  
64 only estimate the NEE by summing  $F_c$  and  $F_s$ , and even a significant number of sites  
65 ignored the  $F_s$ . The  $F_s$  in the vertical gas column within a canopy can be substantial,  
66 requiring attention in NEE estimates (Aubinet et al., 2000). The  $F_s$  contributes ~60% to  
67 nocturnal turbulent flux underestimation in forest ecosystems with “ideal” topography  
68 (Mchugh et al., 2017). Especially, during atmospherically stable periods such as the  
69 early morning, sunset, and nighttime transitions, the  $F_s$  has a significant impact on the  
70 NEE. For 30-min ecosystem carbon flux measurements, ignoring  $F_s$  would  
71 underestimate the NEE (Zhang et al., 2010). The  $F_s$  value typically ranges from  $-2$  to  
72  $-5 \mu\text{mol m}^{-2} \text{s}^{-1}$  in the early morning, and the  $F_s$  is about  $1-3 \mu\text{mol m}^{-2} \text{s}^{-1}$  after sunset  
73 for temperate forests. The effect of the  $F_s$  on the NEE of forest ecosystems decreases  
74 with the increase of timescale (Li et al., 2020). However, neglecting the  $F_s$  value can  
75 lead to a misunderstanding of the CO<sub>2</sub> exchange processes, such as ecosystem  
76 respiration and photosynthesis, and their relationship with key control factors such as

77 solar radiation, temperature, and moisture (Mchugh et al., 2017). Therefore, it is  
78 imperative not to overlook  $F_s$  to ensure more precise NEE estimates of forest  
79 ecosystems, particularly in complex terrains.

80 Despite the challenges inherent in monitoring forest conditions, understanding the  
81 carbon flux of forest ecosystems in complex terrains or with heterogeneous underlying  
82 surfaces remains an area of great interest. Topography complexity plays a complex role  
83 in the transportation of momentum, energy, and mass in the atmospheric boundary layer,  
84 with direct impacts on the airflow patterns, spatiotemporal characteristics, and gas  
85 concentration fluctuations (Sha et al., 2021; Finnigan et al., 2020). Differences in  
86 airflow along the slope, lateral  $\text{CO}_2$  discharge downhill, and spatiotemporal variations  
87 in soil respiration result in the  $\text{CO}_2$  outflow from slopes and valleys lagging behind the  
88 flat top of the mountain (De Araújo et al., 2010). At night, under stable atmospheric  
89 stratification, cold air moves from valley forest canopy to the ground the and then flows  
90 to low-lying areas, causing a “carbon pooling” effect. The gradient of  $[\text{CO}_2]$  below the  
91 EC sensors fluctuates significantly, and the cold air discharge above the canopy reduces  
92  $\text{CO}_2$  storage, leading to an underestimation of forest ecosystem respiration (Yao et al.,  
93 2011; De Araújo et al., 2008; De Araújo et al., 2010).

94 According to the theoretical definition,  $F_s$  estimates are derived by averaging the  
95  $[\text{CO}_2]$  of the control volume at the beginning and the end of the EC averaging period  
96 (30 min or 1 h) and dividing by the EC averaging period (Finnigan, 2006). The  
97 estimation of  $F_s$  at numerous sites frequently employs a vertical profile system. This  
98 approach operates under the assumption that the  $F_s$  represents the integration of the time

99 derivative of the vertically determined column-averaged  $[\text{CO}_2]$ . It is noteworthy that  
100 the column-averaged  $[\text{CO}_2]$  may not accurately represent the average  $[\text{CO}_2]$  of the  
101 control volume in cases of inadequate air mixing, leading to insufficient sampling.  
102 Previous study showed that relying solely on tower-top measurements can lead to  
103 underestimation of  $F_s$  by up to 34% compared to the eight-level profile approach (Gu  
104 et al., 2012). The NEE magnitude with the  $F_s$  based on the 2-min  $[\text{CO}_2]$  averaging time  
105 window (instantaneous concentration approach) was found to be 5% higher than that of  
106 the 30-min-window-based  $F_s$  (averaging concentration approach), particularly during  
107 nighttime in the growing season (Wang et al., 2016). A proper measuring system with  
108 improving the horizontal representativeness can reduce the bias of  $F_s$  to 2–10%  
109 (Nicolini et al., 2018). Most research has examined how vertical and horizontal gas  
110 concentration sampling point distribution affects the uncertainty in  $F_s$  estimation  
111 (Bjorkegren et al., 2015; Wang et al., 2016; Yang et al., 2007; Yang et al., 1999), with a  
112 small number of studies examining the effect of  $[\text{CO}_2]$  sampling frequency on the  $F_s$   
113 (Finnigan, 2006; Heinesch et al., 2007). Certain studies have experimentally validated  
114 new concepts, such as correlating the gas sampling point concentration with the  
115 horizontal distribution (Nicolini et al., 2018). Some studies have approached the true  
116 value theoretically, such as through defining the control volume represented by flux  
117 measurements (Metzger, 2018; Xu et al., 2019). However, the number of complete  
118 column samples required to describe the column-averaged  $[\text{CO}_2]$  of each 30-min or 1-  
119 h  $F_s$  estimate is still undetermined.

120 Previous studies have emphasized the significance of the  $F_s$  to the NEE and the

121 influence of [CO<sub>2</sub>] dynamics on F<sub>s</sub> estimates in complex terrains. To overcome any  
122 disparities between sensors and obtain precise changes in the [CO<sub>2</sub>] gradient above and  
123 below the forest canopy, individual gas analyzers are extensively utilized to measure  
124 [CO<sub>2</sub>] levels vertically (Siebicke et al., 2011). However, a single gas analyzer introduces  
125 time delays when monitoring multi-point [CO<sub>2</sub>] curves. Accurately determining the F<sub>s</sub>  
126 estimates can be challenging due to the spatial and temporal resolution of [CO<sub>2</sub>]  
127 measurements (Wang et al., 2016). The random error of the F<sub>s</sub> estimates using one  
128 complete column sample is considerably high due to short-term [CO<sub>2</sub>] fluctuations  
129 (Nicolini et al., 2018). The calculation of the F<sub>s</sub> using time-averaged [CO<sub>2</sub>] profiling  
130 leads to significant information loss at high frequency, resulting in a substantial  
131 underestimation bias. Furthermore, resource constraints in the measurement system  
132 leads to the gap that the systematic bias and random error in F<sub>s</sub> estimate are  
133 irreconcilable. This issue necessitates further efforts to characterize [CO<sub>2</sub>] fluctuations  
134 across different sites and demonstrate the mechanisms influencing F<sub>s</sub> magnitudes,  
135 uncertainties, and their contributions to NEE observations in complex terrains. Thus,  
136 this manuscript aims to bridge this gap by introducing a statistical method to estimate  
137 F<sub>s</sub> values and their uncertainties.

138 This paper employed an innovative EC site with three flux towers (Qingyuan-Ker  
139 Towers) to monitor three typical types of temperate forest stands located in complex  
140 terrains in northeastern China. This study introduces a decision-level fusion model  
141 based on weighing the underestimation bias and random error of the F<sub>s</sub> to obtain more  
142 accurate results. The objectives of this study were to: 1) compare diurnal, seasonal, and

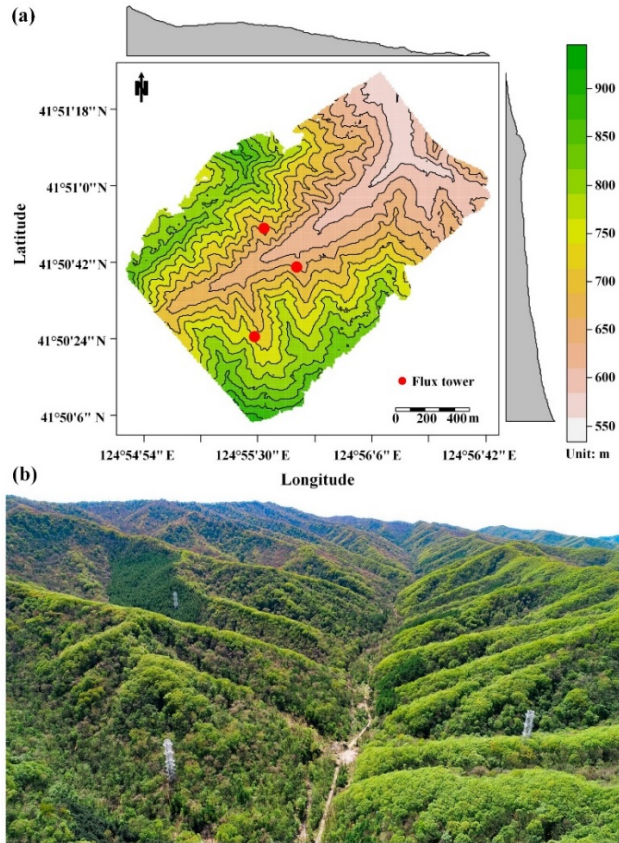
143 spatial differences in  $[\text{CO}_2]$  fluctuations,  $F_s$ , and its uncertainty; 2) examine the  
144 variation in  $F_s$  uncertainty with different  $[\text{CO}_2]$  averaging time windows; and 3)  
145 investigate the response of  $F_s$  and its uncertainty to  $[\text{CO}_2]$  fluctuations, wind above the  
146 canopy, and terrain complexity, and quantify the impact of the  $F_s$  on the NEE estimates  
147 under these conditions.

## 148 **2 Materials and methods**

### 149 **2.1 Study site and instrumental set-up**

150 This study was conducted in temperate forests in a watershed based on the Ker  
151 towers (Zhu et al., 2021; Gao et al., 2020), situated in northeast China ( $41^{\circ}50'N$ ,  
152  $124^{\circ}56'E$ ). The region experiences a temperate continental monsoon climate, with an  
153 average annual temperature of  $4.3^{\circ}\text{C}$  and annual rainfall of 758 mm from 2010 to 2021  
154 (Li et al., 2023). The Ker towers consist of three 50-m-high EC towers (Fig. 1) that  
155 observe a mixed broadleaved forest (MBF), a Mongolian oak forest (MOF), and a Larch  
156 plantation forest (LPF).





157

158 Fig. 1 Overview of the study area. The first map (a) depicts the topography of the study site, with  
 159 black curves indicating elevation contours, and marginal distributions represented as a gray graph,  
 160 averaged over rows and columns. The second image (b) features an aerial photograph of the  
 161 Qingyuan-Ker towers captured in the growing season (Gao et al., 2020).

162 The basic information regarding Ker towers in this study is presented in Table 1.  
 163 The CPEC310 integrated system from Campbell Scientific comprising an EC155  
 164 closed-path infrared gas analyzer (IRGA) and a CSAT3A sonic anemometer, was  
 165 employed to monitor the three-dimensional wind speed and CO<sub>2</sub>/H<sub>2</sub>O concentrations  
 166 (10 Hz). The atmospheric profiling system (AP200, Campbell Scientific Ltd., Logan,  
 167 UT, USA) was utilized to measure the CO<sub>2</sub>/H<sub>2</sub>O concentrations with eight height levels.  
 168 Each level was measured for 15 s (with 10 s for the flushing of the manifold and 5 s for  
 169 logging the average), leading to a measurement cycle of 2 min.

170 Table 1 Basic information of Ker towers

Forest	Mixed broad-leaved	Mongolian oak	Larch plantation
Experiment period	Jan 01, 2020– Dec 31, 2021	Jan 01, 2020– Dec 31, 2021	Jan 01, 2020– Dec 31, 2021
Elevation (m)	634	669	721
Slope (°)	14.8 ± 2.1	19.1 ± 2.9	16.2 ± 5.3
Canopy height (m)	21.5 ± 1.8	13.9 ± 0.6	19.5 ± 0.6
Leaf area indices	3.0 ± 0.5	3.1 ± 0.8	3.9 ± 0.6
Eddy covariance system	CPEC310	CPEC310	CPEC310
Eddy covariance sensor height (m)	46	46	36
Atmospheric profiling system	AP200	AP200	AP200
Profile heights (m)	0.5, 2, 6, 11, 16, 21, 26, 36	0.5, 2, 6, 11, 16, 21, 26, 36	0.5, 2, 6, 11, 16, 21, 26, 36

171 2.2 Calculation of storage flux

172 Averaging the [CO<sub>2</sub>] in a time window was utilized to calculate the F<sub>s</sub> values, in  
 173 addition to data on the air pressure, CO<sub>2</sub>/H<sub>2</sub>O molar fractions, and air temperature at  
 174 different heights above the ground surface (Finnigan, 2006; Montagnani et al., 2018;  
 175 Xu et al., 2019). The molar mixing ratio and mass mixing ratio are conserved quantities  
 176 with the variation of air temperature, air pressure, and water vapor concentration,  
 177 whereas the molar fraction is not. This study determined the F<sub>s</sub> using the molar mixing  
 178 ratio obtained from CO<sub>2</sub>/H<sub>2</sub>O molar fraction observations, applying the ideal gas law  
 179 and Dalton’s partial pressure law (Montagnani et al., 2009). The water vapor molar  
 180 mixing ratio ( $\chi_v$ ) in mmol mol<sup>-1</sup> is given by

$$\chi_v = \frac{c_v}{1 - c_v \times 10^{-3}}, \quad (2)$$

181 where  $c_v$  is the water vapor molar fraction in  $\text{mmol mol}^{-1}$ , and the  $\text{CO}_2$  molar mixing  
 182 ratio ( $\chi_c$ ) in  $\mu\text{mol mol}^{-1}$  is given by

$$\chi_c = \frac{c_c}{1 - c_v \times 10^{-3}}, \quad (3)$$

183 where  $c_c$  is the  $\text{CO}_2$  molar fraction in  $\mu\text{mol mol}^{-1}$ .

184 The dry air density ( $\bar{\rho}_d$ ) in  $\text{mol m}^{-3}$  is calculated as follows:

$$\bar{\rho}_d = \frac{\bar{P}}{(\bar{T} + 273.15) \times (R^* + \chi_v \times 10^{-3} \cdot R^* \cdot M_d/M_v)}, \quad (4)$$

185 where  $R^*$  is the air gas constant ( $8.31441 \text{ Pa m}^3 \text{ K}^{-1} \text{ mol}^{-1}$ ),  $\bar{P}$  is the air pressure in  
 186 Pa, and  $\bar{T}$  is the average air temperature in Celsius.  $M_d$  and  $M_v$  are the dry air and  
 187 water vapor molar mass ( $18.015 \text{ g mol}^{-1}$ ), respectively.  $M_d$  is calculated from the  $\text{CO}_2$   
 188 molar mixing ratio (Khélifa et al., 2007):

$$M_d = 28.9635 + M_c \cdot (\chi_c \times 10^{-6} - 0.0004), \quad (5)$$

189 where  $M_c$  is the carbon molar mass ( $12.011 \text{ g mol}^{-1}$ ).

190 The  $F_s$  estimated from eight-level profiles are calculated as follows:

$$F_s = \bar{\rho}_d \int_0^h \frac{d\bar{\chi}_c}{dt} dz \doteq \bar{\rho}_d \sum_{i=1}^8 \frac{\Delta\bar{\chi}_{c_i} \Delta h_i}{\Delta t}, \quad (6)$$

191 where  $\bar{\chi}_c$  is the average  $\text{CO}_2$  molar mixing ratio and  $\Delta h_i$  is the height represented by  
 192 each level.

193 When measuring the  $F_s$  by sampling  $\text{CO}_2$  at several levels using a single analyzer,  
 194 the synchronous observations of  $\text{CO}_2$  profile are impractical. Consequently, discrete  
 195 temporal sampling and time averaging become necessary. To ensure the temporal  
 196 alignment of  $F_s$  with  $F_c$ , the average  $[\text{CO}_2]$  measurements within the control volume at  
 197 the beginning and end ( $t$ ) of an averaging period (30 min) are calculated by averaging  
 198 over a time window ( $\tau$  min) as follows:

$$\bar{\chi}_{c_i} = \frac{2}{\tau} \sum_{t-\frac{\tau}{2} < t \leq t+\frac{\tau}{2}} \chi_{c_i}(t), \quad (7)$$

199 where  $\tau = 4, 8, \dots, 28$  min. Theoretically, the time window should be kept as short as  
 200 possible in comparison to the turbulence flux averaging period to comply with the  
 201 principle of Reynolds decomposition. We use large windows here for CO<sub>2</sub> averaging in  
 202 an attempt to demonstrate the effects of different window sizes on the accuracy of  
 203 storage flux estimates.

### 204 2.3 Data analysis

205 To evaluate the impact of [CO<sub>2</sub>] fluctuations on F<sub>s</sub> measurements and its  
 206 corresponding uncertainty, empirical modal decomposition (EMD) and Fourier  
 207 spectrum analysis were used to extract the period and amplitude of fluctuations in the  
 208 high-frequency [CO<sub>2</sub>] time series (10 Hz). EMD was used to decompose the [CO<sub>2</sub>] time  
 209 series into intrinsic mode functions based on local signal properties, which yield  
 210 instantaneous frequencies as functions of time, allowing for the identification of  
 211 embedded structures of eddies. EMD is applicable to non-linear and non-stationary  
 212 processes (Huang et al., 1998). The period and amplitude of [CO<sub>2</sub>] fluctuations above  
 213 the forest canopies reflected the eddy size. Subsequently, the maximum period and  
 214 amplitude of [CO<sub>2</sub>] fluctuations in a short term (2h) was indicative of large eddies under  
 215 the influence of gust.

216 Due to the diurnal and seasonal variability of flux measurements, this study  
 217 defined the transition period and growing season. The solar elevation angle was used  
 218 to define the transition period as 1-h before sunrise (sunset) to 2-h after sunrise (sunset).

219 The growing degree days (GDDs) were calculated using the base temperature ( $T_{base}$ ) to  
220 determine the beginning and end of the growing season, and the formula was as follows  
221 (Mcmaster and Wilhelm, 1997):

$$GDD = \frac{1}{2}(T_{max} + T_{min}) - T_{base}, \quad (8)$$

222 where  $T_{base}$  is 6°C. Considering the persistent demand of temperature to support  
223 vegetation growth, the fourth day of the first GDD greater than zero (less than zero)  
224 over a span of five consecutive days was defined as the starting (ending) time of the  
225 growing season.

226 The main data processing and analysis steps are outlined below:

227 1. EMD and Fourier spectrum analysis of  $[CO_2]$  high-frequency time series were  
228 used to extract the maximum amplitude ( $A_m$ ) and corresponding period ( $P_m$ ) of  $[CO_2]$   
229 fluctuations every 2 h. The data were divided into two subsets based on  $P_m$ , with a cut-  
230 off of 150 s.

231 2.  $CO_2$  storage fluxes were calculated for different  $[CO_2]$  averaging time windows  
232 ( $\tau$ ), ranging from 4 to 28 min in increments of 4 min.

233 3. The standardized major axis (SMA) regression model (Warton et al., 2012) was  
234 used to compare the slope differences (bias) between  $F_{s_\tau}$  and  $F_{s_{28}}$  for different  $P_m$  and  
235 the forest stands. The SMA model offers routines for comparing parameters  $a$  and  $b$   
236 among groups for symmetric problems.

237 4. The normalized root mean square error (NRMSE) and slope were used to  
238 evaluate the relative error and bias between  $F_{s_\tau}$  and  $F_{s_{28}}$ . The NRMSE is calculated as  
239 follows:

$$NRMSE = 100 \times \sqrt{\frac{\sum_{i=1}^N (F_{s,\tau}^{(i)} - F_{s,28}^{(i)})^2}{\sum_{i=1}^N (F_{s,28}^{(i)} - \overline{F_{s,28}})^2}} \quad (9)$$

240 where  $i$  indicates the  $i^{\text{th}}$  observation.

241 5. The normalized weighting coefficient ( $w$ ) of  $F_{s,\tau}$  was estimated based on the  
 242 NRMSE and slope (Wang et al., 2020). The details are shown in Appendix A1. Then,  
 243 using the decision-level fusion model,  $F_{s,\text{comb}}$  was calculated as follows:

$$F_{s,\text{comb}} = w_1^* \cdot F_{s,4} + w_2^* \cdot F_{s,8} + \dots + w_7^* \cdot F_{s,28} \quad (10)$$

244 The decision-level fusion model automatically assigned weights to the  $F_s$  based on  
 245 different  $[\text{CO}_2]$  averaging time windows. Its purpose in this study was to balance the  
 246 relative error and bias of  $F_s$  estimates caused by  $[\text{CO}_2]$  sampling. The analysis was  
 247 performed using the EMD and smatr R packages (Warton et al., 2012; Huang et al.,  
 248 1998).

#### 249 2.4 Uncertainty analysis

250 To improve the accuracy of estimating the uncertainty of  $F_s$  using individual tower,  
 251 this work has made modifications to the 24-h difference method by extending the  
 252 sampling time windows and applying meteorological condition constraints (Hollinger  
 253 and Richardson, 2005). This method trades time for space to estimate the uncertainty  
 254 of  $F_s$ . To determine the uncertainty of  $F_s$ , expressed as  $\sigma(\varepsilon_s)$ , in this case, we compared  
 255 the observations at moment  $i$  within a day to the average of several observations during  
 256 a similar period and with similar meteorological conditions. The specific computations  
 257 were as follows:

$$\bar{F}_s^{(i)} = \frac{1}{N} \sum_{t \in \Omega, \lambda_t \in \Lambda} I(\lambda_t) \cdot F_s^{(t)}, \quad (11)$$

$$\Lambda = \{\lambda_t | \sqrt{\frac{(u_*^{(\lambda_t)} - u_*^{(i)})^2}{\sigma_{u_*}} + \frac{(\text{Ta}(\lambda_t) - \text{Ta}^{(i)})^2}{\sigma_{\text{Ta}}} + \frac{(\text{H}(\lambda_t) - \text{H}^{(i)})^2}{\sigma_{\text{H}}}} < \delta\}, \quad (12)$$

$$\varepsilon_s^{(i)} = F_s^{(i)} - \bar{F}_s^{(i)}, \quad (13)$$

$$\bar{\varepsilon}_s^{(i)} = \frac{1}{N} \sum_{t \in \Omega, \lambda_t \in \Lambda} I(\lambda_t) \cdot \varepsilon_s^{(t)}, \quad (14)$$

$$\sigma(\varepsilon_s)^{(i)} = \sqrt{\frac{1}{N} \sum_{t \in \Omega, \lambda_t \in \Lambda} I(\lambda_t) \cdot (\varepsilon_s^{(t)} - \bar{\varepsilon}_s^{(i)})^2}, \quad (15)$$

258 where  $\Omega$  was the moment interval ( $i-0.5$  h,  $i+0.5$  h) within a certain time window (15  
 259 d);  $I$  was indicator function; the set  $\Lambda$  represented consisted of elements that meet  
 260 similar meteorological conditions, including the  $u_*$ , air temperature (Ta), and sensible  
 261 heat flux (H);  $\sigma_{u_*}$ ,  $\sigma_{\text{Ta}}$ , and  $\sigma_{\text{H}}$  are the standard deviation of the  $u_*$ , Ta, and H,  
 262 respectively;  $\delta$  was the threshold of Euclidean distance; and  $\varepsilon_s$  was the random error  
 263 of  $F_s$ .

264 After estimating the uncertainty of  $F_s$ , this study extended the work conducted by  
 265 Richardson et al. (2008) to analyze its relationship with the magnitude of flux  
 266 measurements ( $|F_s|$ ),  $[\text{CO}_2]$  fluctuations ( $A_m$  and  $P_m$ ),  $u_*$ , and terrain complexity index  
 267 (TCI). A comprehensible description of the TCI can be found in Appendix A2. This  
 268 relationship can be approximated by using the following equation:

$$\sigma(\varepsilon_s) = \beta_0 + \sum_{i=1} \beta_i \cdot x_i, \quad (16)$$

269 where the nonzero intercept term  $\beta_0$  indicates the size of the random uncertainty as  
 270  $x_i$  approaches 0, which varies with the observation site, with larger value of  $\beta_0$

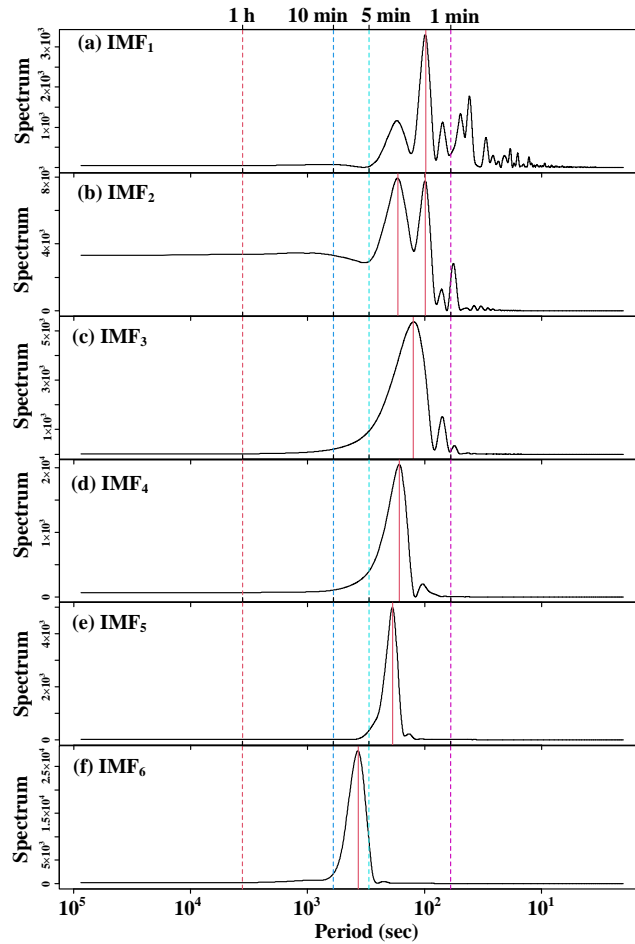
271 indicating greater uncertainty. The slope term  $\beta_i$  indicates the sensitivity of the size of  
272 the random uncertainty of  $x_i$ , with smaller  $\beta_i$  values indicating a probability  
273 distribution of uncertainty closer to white noise.

## 274 **3 Results**

### 275 3.1 Characterization of [CO<sub>2</sub>] fluctuation and F<sub>s</sub> variations

276 The [CO<sub>2</sub>] high-frequency time series above the forest canopies were decomposed  
277 using EMD, followed by spectral analysis to extract the fluctuation period and  
278 amplitude of [CO<sub>2</sub>] at different time scales. As depicted in Fig. 2, it became evident that  
279 the [CO<sub>2</sub>] above the canopies displayed short-term fluctuations with periods ranging  
280 from 1 to 10 min, and the amplitude of these fluctuations showed an increasing trend  
281 with longer periods. This observation strongly suggested the presence of large eddies  
282 influenced by gusts above the canopies, and these eddies were responsible for the  
283 increasing amplitude of [CO<sub>2</sub>] fluctuations as their size increased.





284

285 Fig. 2 Power spectral density of the intrinsic mode function (IMF) of above-canopy CO<sub>2</sub>  
 286 concentrations in the Mongolian oak forest on July 2, 2020 (24 h).

287 To examine the spatio-temporal variations in large eddies, this study compared the  
 288  $A_m$  and  $P_m$  values above canopies across different forest stands. The analysis utilized  
 289 data from daytime, nighttime, and transition periods in both the growing and dormant  
 290 seasons. The averages of  $A_m$  and  $P_m$  averages for the above-canopy [CO<sub>2</sub>] in the three  
 291 forest stands ranged from 1.588 to 136.667 ppm and from 2.313 to 2.784 min,  
 292 respectively (Table 2). Fig. 3 demonstrated significant seasonal and diurnal differences  
 293 ( $P < 0.01$ ) in  $P_m$ , with higher values during daytime in the growing season, and lower  
 294 values during the daytime in the dormant season. Moreover,  $P_m$  was significantly  
 295 different ( $P < 0.01$ ) among different forest stands during the same time period, with

296 MBF stand having the highest values, followed by the MOF, and the lowest values in  
 297 the LPF. During the growing season, the  $A_m$  values were significantly higher than those  
 298 during the dormant season, with both daytime and nighttime values also exhibiting  
 299 significant differences ( $P < 0.01$ ) among different forest stands. This observation  
 300 provided evidence of significant spatio-temporal variability in large eddies influenced  
 301 by gusts.

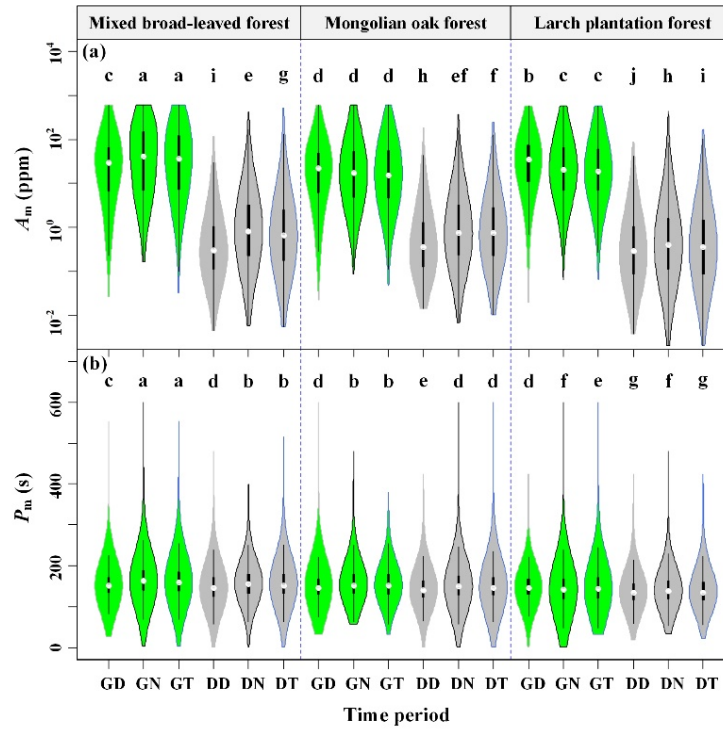
302 Table 2 Mean of the  $A_m$  and  $P_m$  in different forest stands at different periods

Variable	Tower site	Growing season			Dormant season		
		DT <sup>1</sup>	NT <sup>2</sup>	TP <sup>3</sup>	DT	NT	TP
$A_m$ <sup>4</sup> (ppm)	MBF <sup>6</sup>	57.932	<b>139.667</b>	136.717	2.219	5.212	4.944
	MOF <sup>7</sup>	36.160	57.945	55.777	2.699	5.175	4.637
	LPF <sup>8</sup>	52.688	58.816	60.147	<b>1.588</b>	2.985	2.456
$P_m$ <sup>5</sup> (s)	MBF	154.563	<b>167.024</b>	164.824	158.449	151.428	158.121
	MOF	151.986	160.633	159.146	153.091	147.491	153.274
	LPF	149.003	143.950	145.696	143.458	<b>138.794</b>	142.009

303 <sup>1</sup> DT represents daytime; <sup>2</sup> NT represents nighttime; <sup>3</sup> TP represents transition period. <sup>4</sup>  $A_m$   
 304 represents the maximum amplitude of short-term CO<sub>2</sub> concentration fluctuations; <sup>5</sup>  $P_m$  represents  
 305 the corresponding period of maximum amplitude. <sup>6</sup> MBF represents mixed broad-leaved forest; <sup>7</sup>  
 306 MOF represents Mongolian oak forest; <sup>8</sup> LPF represents Larch plantation forest.

307 To estimate the uncertainty of  $F_s$  using an individual tower, a comprehensive  
 308 analysis of its diurnal and seasonal dynamics, as well as the functional relationship  
 309 between  $F_s$  and  $u^*$ , was necessary. Fig. 4 presented significant diurnal variations and  
 310 seasonal differences in  $F_s$  across the three forest stands. During the growing season, the  
 311 median diurnal variation of  $F_s$  for the three forest stands ranged from  $-2.960$  to  $2.647$   
 312  $\mu\text{mol m}^{-2} \text{s}^{-1}$ , whereas during the dormant season, it ranged from  $-1.306$  to  $1.012$   $\mu\text{mol}$   
 313  $\text{m}^{-2} \text{s}^{-1}$ . Comparing the extent of  $F_s$  diurnal variation among the three forest stands,

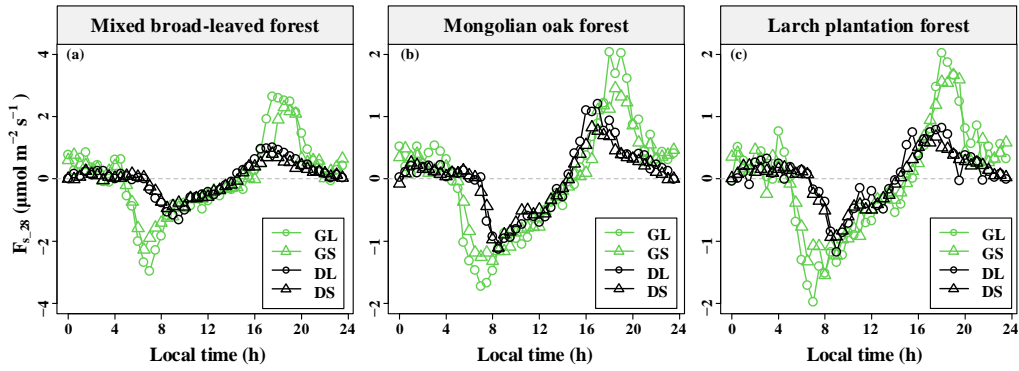
314 MBF exhibited the largest extent during the growing season, while the extent of the  
 315 three forest stands were similar during the dormant season. Notably, it was observed  
 316 that the amplitudes for longer  $P_m$  values were greater than those for shorter  $P_m$  values.  
 317 This observation indicated that the larger the eddies, the greater the magnitude of  $F_s$ .



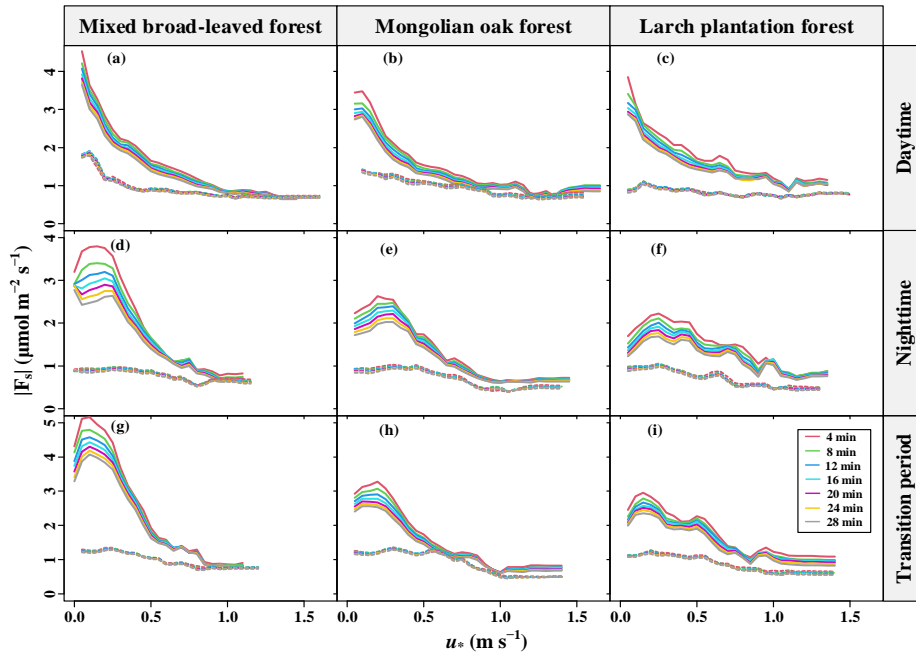
318  
 319 Fig. 3 Maximum amplitude ( $A_m$ ) (a) and corresponding period ( $P_m$ ) (b) of short-term  $CO_2$   
 320 concentration fluctuations in different forest stands for seasonal and diurnal variations, where GD,  
 321 GN, GT, DD, DN, and DT denote the growing season daytime, growing season nighttime,  
 322 growing season transition period, dormant season daytime, dormant season nighttime, and  
 323 dormant season transition period, respectively. Columns with different lowercase letters are  
 324 significantly different ( $P < 0.05$ ) according to Fisher's least significant difference test.

325 Furthermore, a  $u^*$  threshold value was identified for the variation of  $F_s$  with  $u^*$   
 326 during daytime in both the dormant and growing seasons (Fig. 5). When  $u^*$  fell below  
 327 the  $u^*$  threshold, the magnitude of  $F_s$  ( $|F_s|$ ) decreased with increasing  $u^*$ . Conversely,  
 328 when  $u^*$  exceeded the  $u^*$  threshold, the  $|F_s|$  tended to remain relatively constant. Notably,  
 329 a maximum point for the  $|F_s|$  was observed when the  $u^*$  was less than 0.5 m/s during the

330 growing season, whereas not during the dormant season. This phenomenon was  
 331 particularly evident during the nighttime and transition periods of the growing season,  
 332 where  $|F_s|$  exhibited an initial increase followed by a subsequent decrease with  $u^*$ . These  
 333 observations strongly indicated that the effect of the turbulent mixing strength on the  
 334  $|F_s|$  over complex terrains was nonlinear and exhibited diurnal and seasonal differences.



335  
 336 Fig. 4 Median diurnal variation of CO<sub>2</sub> storage flux ( $F_s$ ) based on 28-min CO<sub>2</sub> concentration  
 337 averaging time windows in the three forest stands during different seasons. GS indicates the  
 338 growing season and a short period of maximum amplitude ( $P_m$ ), GL indicates the growing season  
 339 and a long  $P_m$ , DS indicates the dormant season and a short  $P_m$ , and DL indicates the dormant  
 340 season and a long  $P_m$ .



341  
 342 Fig. 5 Magnitudes of CO<sub>2</sub> storage flux ( $|F_s|$ ) determined with different CO<sub>2</sub> concentration average  
 343 time windows as a function of the friction velocity ( $u^*$ ) and moving block averages from all 30-

344 min data for the years 2020-2021. Dashed and solid lines indicate the dormant and growing  
345 seasons, respectively.

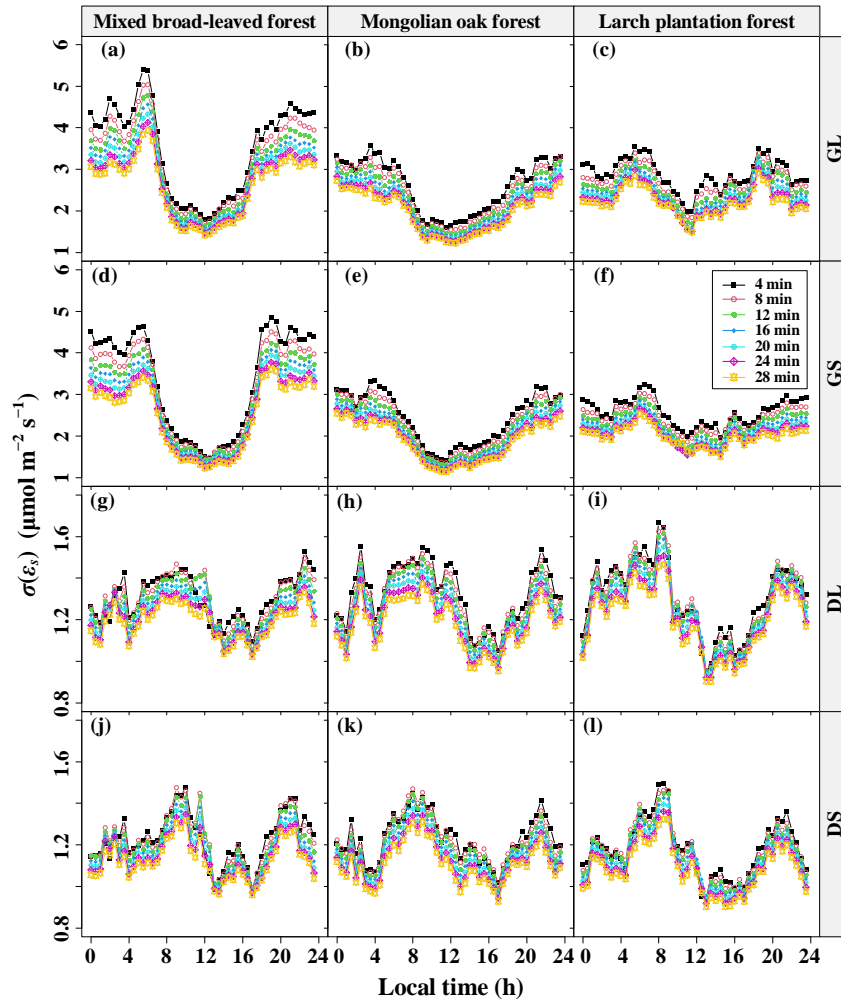
### 346 3.2 Effect of [CO<sub>2</sub>] fluctuations on the F<sub>s</sub> and its uncertainty

347 To investigate the influence of the [CO<sub>2</sub>] fluctuation periods on the error of F<sub>s</sub>  
348 measurement, this study computed the diurnal average of the standard deviation  $\sigma(\varepsilon_s)$   
349 of the 30-min F<sub>s</sub> uncertainty ( $\varepsilon_s$ ) separately for different  $P_m$  values and the seasons. The  
350 overall distribution of  $\varepsilon_s$  showed a non-normal distribution with a high peak (kurtosis >  
351 2 and  $P < 0.05$ , results presented in Supplementary Table 1–4). The daily variation  
352 curves of  $\sigma(\varepsilon_s)$  at various [CO<sub>2</sub>] averaging time windows are presented in Fig. 6. It  
353 was observed that the diurnal variation range of  $\sigma(\varepsilon_s)$  was higher during the growing  
354 season compared to the dormant season, regardless of the  $P_m$  lengths, indicating a  
355 seasonal difference independent of the  $P_m$ . Additionally, during the growing season,  
356 both MBF and MOF demonstrated evident diurnal variation in  $\sigma(\varepsilon_s)$ , with the peak  
357 occurring at night and the trough during the daytime. The diurnal variation range of  
358  $\sigma(\varepsilon_s)$  varied across the three forest stands, with MBF exhibiting the largest amplitude.

359 Furthermore, a significantly positive correlation was observed between  $\sigma(\varepsilon_s)$  the  
360 |F<sub>s</sub>| ( $P < 0.01$ ), with site, seasonal, and diurnal differences (Fig. 7). The relationship  
361 between these variables was characterized by intercepts and slopes that varied across  
362 different [CO<sub>2</sub>] averaging time windows, ranging from 1.99 to 2.82 and from 0.24 to  
363 0.28, respectively (results presented in the Supplementary Tables 5–6). Both decreased  
364 as the [CO<sub>2</sub>] averaging time window increased, with the growing season exhibiting  
365 larger values compared to the dormant season (results shown in the Supplementary

366 Tables 5–6). These findings suggested that increasing the [CO<sub>2</sub>] averaging time window,  
367 results in a reduction of the random error in F<sub>s</sub> and the correlation coefficient between  
368  $\sigma(\varepsilon_s)$  and |F<sub>s</sub>|. This indicated a decrease in variability of  $\sigma(\varepsilon_s)$  and a behavior similar  
369 to white noise.

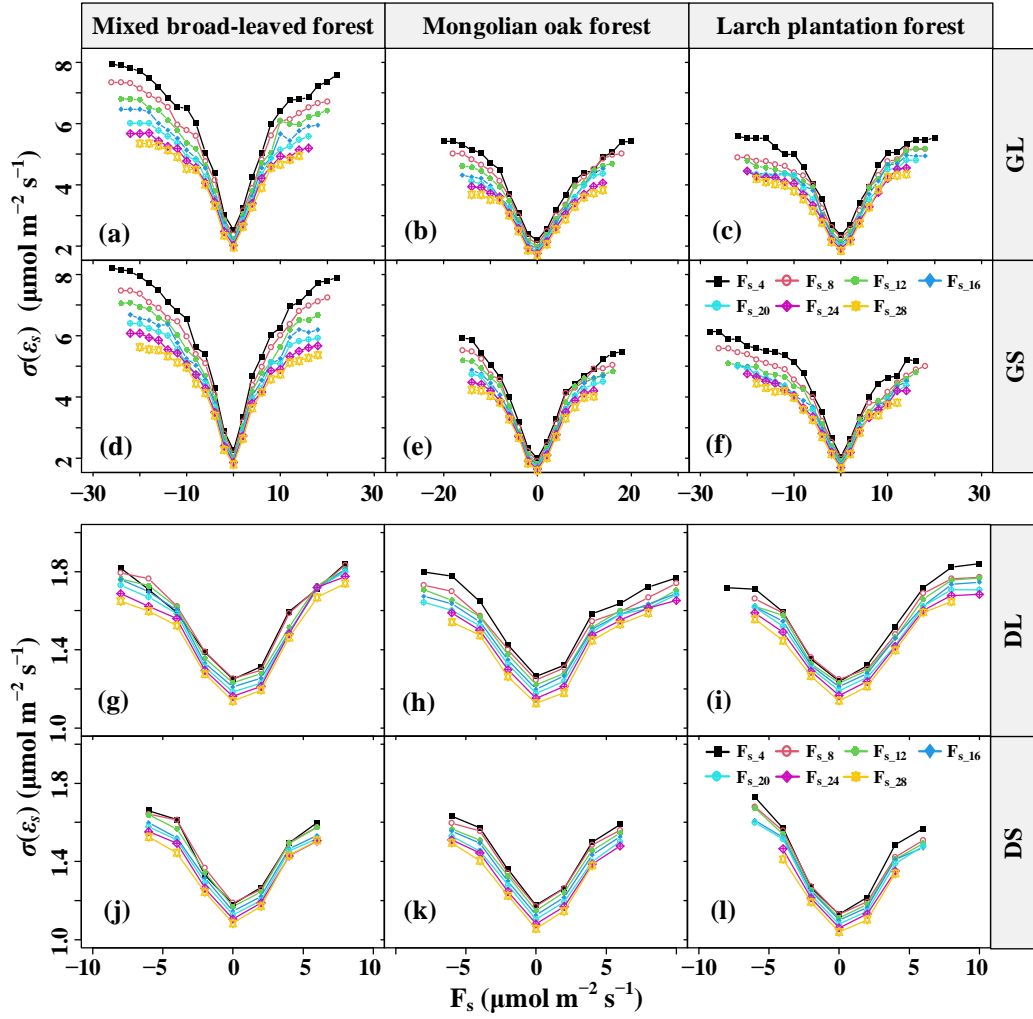
370 To assess the impact of [CO<sub>2</sub>] fluctuations on the error and bias of F<sub>s</sub> measurement,  
371 this study compared the NRMSE and slopes of F<sub>s</sub> based on different [CO<sub>2</sub>] averaging  
372 time windows, with reference to the baseline F<sub>s,28</sub>, across various *P<sub>m</sub>* values, time  
373 periods, and sites. As shown in Fig. 8, the NRMSE decreased and approached  
374 convergence as the [CO<sub>2</sub>] averaging time windows increased. During both daytime and  
375 nighttime in the growing season, the NRMSE corresponding to longer *P<sub>m</sub>* was greater  
376 than that corresponding to shorter *P<sub>m</sub>*, while the opposite trend was observed during the  
377 dormant season. Additionally, the longer the [CO<sub>2</sub>] averaging time window, the greater  
378 the relative underestimation of F<sub>s</sub>.



379

380 Fig. 6 Diurnal variations in the random uncertainty ( $\sigma(\varepsilon_s)$ ) of CO<sub>2</sub> storage flux ( $F_s$ ) errors ( $\varepsilon_s$ ) at  
 381 different CO<sub>2</sub> concentration ( $[CO_2]$ ) averaging time windows and their seasonal differences, where

382 GS indicates the growing season and a short period of maximum amplitude ( $P_m$ ) of  $[CO_2]$   
 383 fluctuations, GL indicates the growing season and a long  $P_m$ , DS indicates the dormant season and  
 384 a short  $P_m$ , and DL indicates the dormant season and a long  $P_m$ .



385

386

387

388

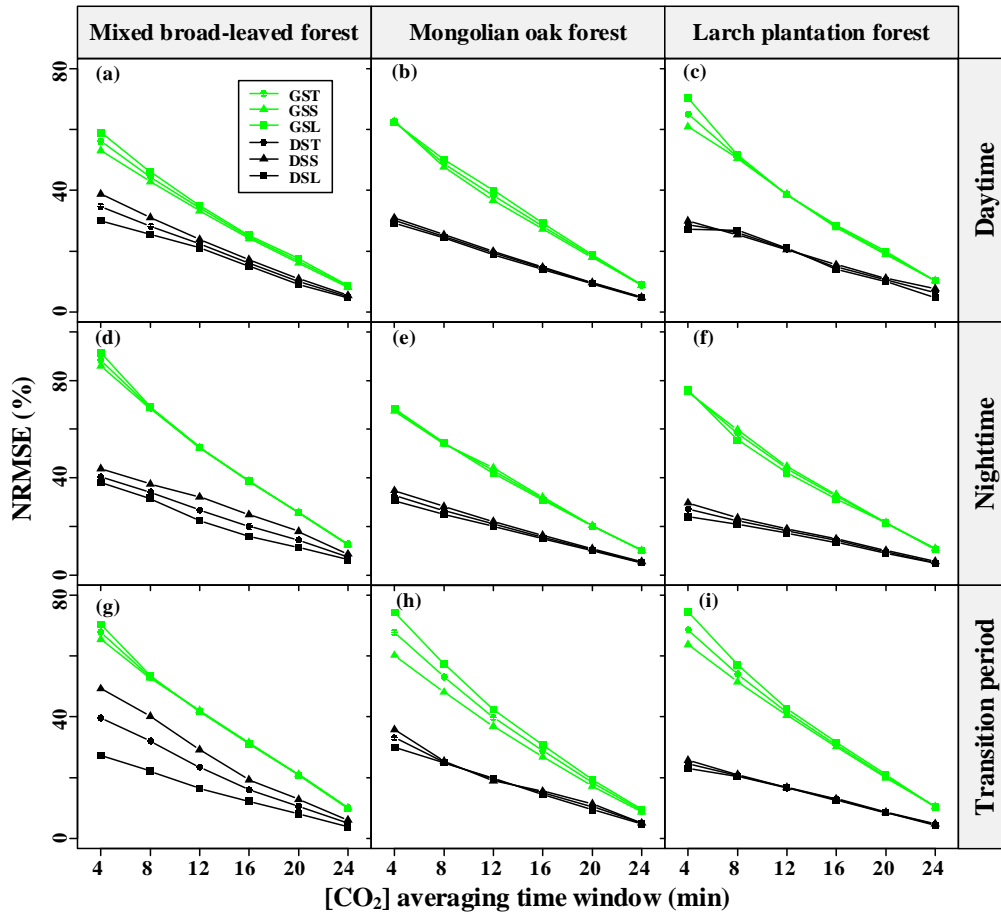
389

390

391

Fig. 7 Random uncertainty  $\sigma(\varepsilon_s)$  of  $\text{CO}_2$  storage flux ( $F_s$ ) errors ( $\varepsilon_s$ ) at different  $\text{CO}_2$  concentration ( $[\text{CO}_2]$ ) averaging time windows as a function of the  $F_s$  magnitude for mixed broad-leaved forest, Mongolian oak forest, and Larch plantation forest during the growing and dormant seasons. GS indicates the growing season and a short period of maximum amplitude ( $P_m$ ) of  $[\text{CO}_2]$  fluctuations, GL indicates the growing season and a long  $P_m$ , DS indicates the dormant season and a short  $P_m$ , and DL indicates the dormant season and a long  $P_m$ .





392

393

394

395

396

397

398

399

Fig. 8 Seasonal and diurnal differences in the normalized root mean square error (NRMSE) of  $F_s$  versus the respective  $F_{s,28}$  values for different  $CO_2$  concentration ( $[CO_2]$ ) averaging time windows. GST indicates the growing season and does not distinguish the period of maximum amplitude ( $P_m$ ) of  $[CO_2]$  fluctuations, GSS indicates the growing season and a short  $P_m$ , GSL indicates the growing season and a long  $P_m$ , DST indicates the dormant season and does not distinguish  $P_m$ , DSS indicates the dormant season and a short  $P_m$ , and DSL indicates the dormant season and a long  $P_m$ .

400

401

402

403

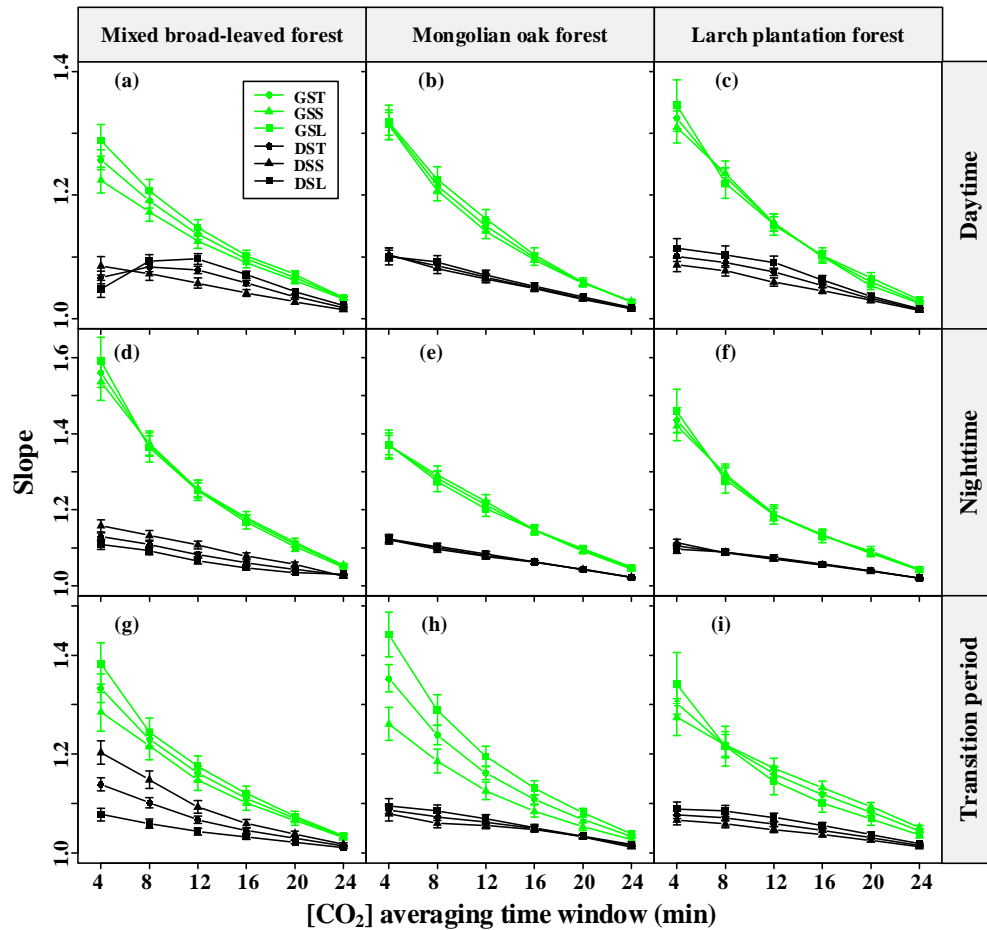
404

405

406

The comparison of slopes between  $F_{s,4}$  and  $F_{s,28}$  in the three forest stands revealed interesting patterns, as depicted in Fig. 9. During the growing season, the slopes corresponding to the shorter  $P_m$  of  $[CO_2]$  fluctuations were consistently lower than those for the longer  $P_m$ , indicating that the effect of  $P_m$  on  $F_s$  uncertainty decreased with increasing  $[CO_2]$  averaging time windows. However, for the MBF stand (Fig. 9d and Fig. 9g), the slopes corresponding to the shorter  $P_m$  of  $[CO_2]$  fluctuations during the dormant season nighttime were actually greater than those for the longer  $P_m$ , primarily

407 due to diurnal variations in the daily dynamics of  $F_s$ . Overall, the influence of  $P_m$  on  $F_s$   
 408 uncertainty decreased with increasing  $[CO_2]$  averaging time windows. This suggested  
 409 that averaging  $[CO_2]$  reduced the effect of gusts on the random uncertainty in estimating  
 410  $F_s$ , but led to a systematic underestimation of  $F_s$ .



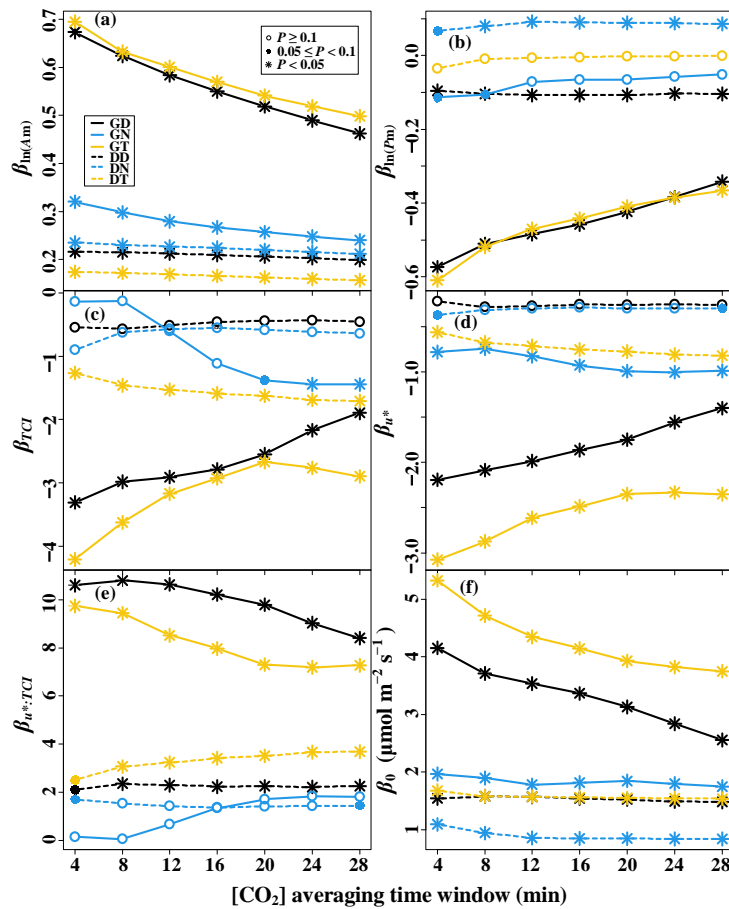
411  
 412 Fig. 9 Seasonal and diurnal differences in the slope of  $CO_2$  storage flux ( $F_s$ ) versus the  $F_{s,28}$  for the  
 413 different  $CO_2$  concentration ( $[CO_2]$ ) averaging time windows. GST indicates the growing season  
 414 and does not distinguish the period of maximum amplitude ( $P_m$ ) cases, GSS indicates the growing  
 415 season and a short  $P_m$ , GSL indicates the growing season and a long  $P_m$ , DST indicates the  
 416 dormant season and does not distinguish  $P_m$ , DSS indicates the dormant season and a short  $P_m$ ,  
 417 and DSL indicates the dormant season and a long  $P_m$ .

418 To analyze the effect of  $[CO_2]$  fluctuations on  $|F_s|$  in complex terrains, this study  
 419 developed a multiple linear regression model, considering the interaction effects of  
 420 turbulent mixing and terrain complexity on  $|F_s|$ , as shown in Fig. 10.  $A_m$  exhibited a

421 significant positive correlation with  $|F_s|$  in all time periods ( $P < 0.05$ ). Conversely,  $P_m$   
422 showed a significant negative correlation with  $|F_s|$  during the dormant season daytime,  
423 the growing season daytime, and the transition periods ( $P < 0.05$ ). Additionally, their  
424 correlation coefficient decreased with increasing  $\tau$ . In Fig. 10d and Fig. 10e, a  $u^*$   
425 threshold was observed during the growing season nighttime. When the  $u^*$  was below  
426 the threshold, higher TCI values resulted in smaller  $|F_s|$ ; whereas when the  $u^*$  was above  
427 the threshold, higher TCI values led to larger  $|F_s|$ . During the growing season nighttime  
428 and transition periods,  $u^*$  showed a significant negative correlation ( $P < 0.05$ ) with  $|F_s|$ ,  
429 and the correlation coefficient decreased with increasing TCI values. These  
430 observations suggested that the effect of turbulent mixing on the  $|F_s|$  uncertainty was  
431 regulated by terrain complexity.

432 A multiple linear regression model was used to analyze the effect of  $[CO_2]$   
433 fluctuations on the random uncertainty of  $F_s$ ,  $\sigma(\varepsilon_s)$ , in complex terrains. This model  
434 considered the interaction effects of  $[CO_2]$  fluctuations and terrain complexity on  
435  $\sigma(\varepsilon_s)$ , as shown in Fig. 11. As evident from Fig. 11a and Fig. 11e, the  $A_m$  exhibited a  
436 significant positive correlation ( $P < 0.05$ ) with  $\sigma(\varepsilon_s)$  during both the dormant season's  
437 nighttime and the growing season. Throughout the transition period of the growing  
438 season,  $P_m$  displayed a significant negative correlation with  $\sigma(\varepsilon_s)$  ( $P < 0.05$ ). The  
439 magnitude of these correlation coefficients decreased with the increasing  $[CO_2]$   
440 averaging time windows. During the transition period of the dormant season, a TCI  
441 threshold was observed, with  $P_m$  showing a significant positive correlation ( $P < 0.05$ )  
442 with  $\sigma(\varepsilon_s)$  when the TCI was below the threshold, and a significantly negative

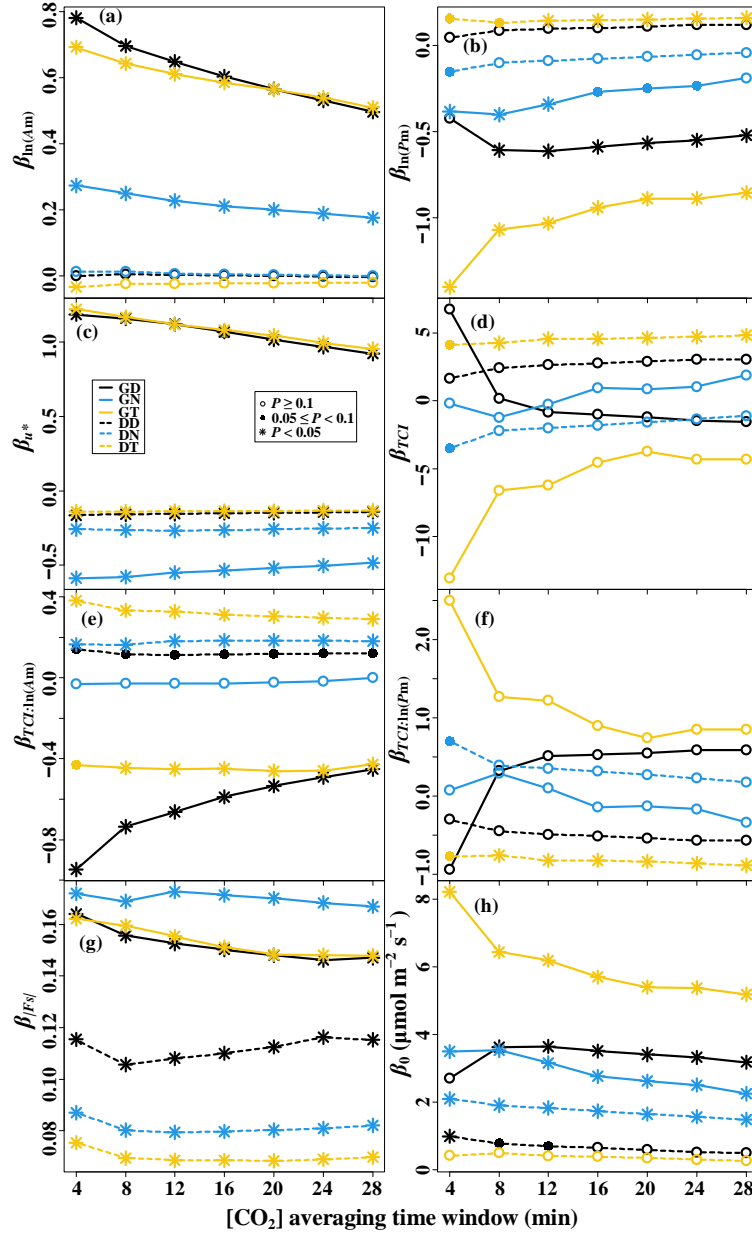
443 correlation ( $P < 0.05$ ) with  $\sigma(\varepsilon_s)$  when the TCI exceeded the threshold (Fig. 11b and  
 444 Fig. 11f). The  $u^*$  showed a significantly negative correlation with  $\sigma(\varepsilon_s)$  during the  
 445 daytime and transition periods of the growing season ( $P < 0.05$ ), while in other time  
 446 periods,  $u^*$  was significantly positively correlated with  $\sigma(\varepsilon_s)$  ( $P < 0.05$ ). The  $|F_s|$   
 447 demonstrated a significant positive correlation with  $\sigma(\varepsilon_s)$  ( $P < 0.05$ ) in all time  
 448 periods, with its correlation coefficient being greater during the growing season than  
 449 during the dormant season. These observations suggested that the relationship between  
 450 the random uncertainty in  $F_s$  and  $[\text{CO}_2]$  fluctuations was moderated by topographic  
 451 complexity. Increasing the  $[\text{CO}_2]$  averaging time window reduced the effect of  $[\text{CO}_2]$   
 452 fluctuations on the random uncertainty in  $F_s$ .



453

454 Fig. 10 Linear regression coefficients of the  $\text{CO}_2$  storage flux ( $F_s$ ) magnitude—driving factors

455 relationships for the seven CO<sub>2</sub> concentration ([CO<sub>2</sub>]) averaging time windows. The predictors of of  
 456 the multiple linear models are (a) the logarithm of maximum amplitude of [CO<sub>2</sub>] fluctuations  
 457 (ln(A<sub>m</sub>)), (b) the logarithm of the corresponding period of maximum amplitude (ln(P<sub>m</sub>)), (c) the  
 458 terrain complexity index (TCI), (d) the friction velocity (u\*), and (e) the interaction term of TCI  
 459 and u\*, respectively. (f) β<sub>0</sub> represents the intercept term.



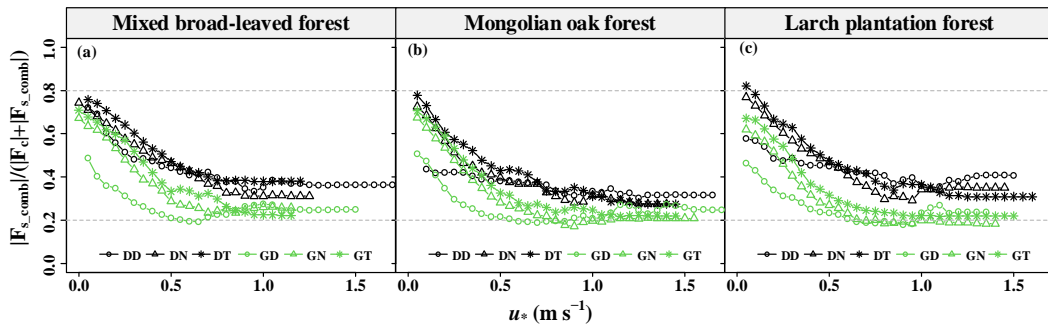
460

461 Fig. 11 Linear regression coefficients of the random uncertainty of CO<sub>2</sub> storage flux ( $\sigma(\varepsilon_s)$ )—  
 462 driving factors relationships determined with Eq. (11) for the seven CO<sub>2</sub> concentration ([CO<sub>2</sub>])  
 463 averaging time windows. The predictors of the multiple linear models are (a) the logarithm of  
 464 maximum amplitude of [CO<sub>2</sub>] fluctuations (ln(A<sub>m</sub>)), (b) the logarithm of the corresponding period  
 465 of maximum amplitude (ln(P<sub>m</sub>)), (c) the terrain complexity index (TCI), (d) the friction velocity

466 ( $u^*$ ), (e) the interaction term of TCI and  $\ln(A_m)$ , (f) the interaction term of TCI and  $\ln(P_m)$ , and the  
 467 magnitude of storage flux ( $|F_s|$ ), respectively. (h) The intercept term is represented by  $\beta_0$ .

### 468 3.3 Effect of CO<sub>2</sub> storage fluxes uncertainty on NEE observations

469 The 30-min  $F_{s\_comb}$  was obtained by weighing the bias and random error of  $F_s$  using  
 470 different [CO<sub>2</sub>] averaging time windows and  $P_m$  values. This study then focused on the  
 471 magnitude of  $F_{s\_comb}$  in relation to the  $F_c$  magnitude and its diurnal, seasonal, and site  
 472 variations. To assess the significance of  $F_s$  in NEE observations, the relative  
 473 contribution ratio of  $F_{s\_comb}$  magnitude ( $|F_{s\_comb}|/(|F_c|+|F_{s\_comb}|)$ ) was employed. The  
 474  $|F_{s\_comb}|/(|F_c|+|F_{s\_comb}|)$  showed a decreasing trend to convergence with increasing  $u^*$   
 475 (Fig. 12). On average, the  $|F_{s\_comb}|/(|F_c|+|F_{s\_comb}|)$  ranged from 17.2% to 82.0%, with a  
 476 higher value during the dormant season compared to the growing season. This indicated  
 477 that as turbulence intensity increased, the contribution of  $F_s$  to the NEE in forests  
 478 decreased to a constant value. Nevertheless, even under strong turbulence intensity,  $F_s$   
 479 still played a significant role in the NEE observations of forests in complex terrains.



480  
 481 Fig. 12 Relative contribution ratio of the CO<sub>2</sub> storage flux magnitude ( $|F_{s\_comb}|/(|F_c|+|F_{s\_comb}|)$ )  
 482 determined by decision-level fusion model as a function of the friction velocity ( $u^*$ ) moving block  
 483 averages from all 30-min data for the years 2020–2021. GD represents the growing season's  
 484 daytime; GN represents the growing season's nighttime; GT represents the growing season's  
 485 transition period; DD represents the dormant season's daytime; DN represents the dormant  
 486 season's nighttime; DT represents the dormant season's transition period.

487 As indicated in Table 3, both  $P_m$  and TCI exhibited a significant positive

488 correlation with  $|F_{s\_comb}|/(|F_c|+|F_{s\_comb}|)$  ( $P < 0.05$ ), while both  $A_m$  and  $u^*$  showed a  
489 significant negative correlation with  $|F_{s\_comb}|/(|F_c|+|F_{s\_comb}|)$  ( $P < 0.05$ ). Notably,  
490 seasonal variations in correlation coefficients were observed. The correlation between  
491 the  $u^*$  and  $|F_{s\_comb}|/(|F_c|+|F_{s\_comb}|)$  was more pronounced during both the dormant  
492 season's transition period and the growing season, and it decreased with increasing TCI  
493 values during the dormant season's daytime and nighttime.

494 Table 3 Linear regression coefficients of the relative contribution ratio of  $F_{s\_comb}$   
495 magnitudes to NEE observations ( $|F_{s\_comb}|/(|F_c|+|F_{s\_comb}|)$ ) —driving factors  
496 relationships for the six time periods.

Time period	$\beta_0$	$\ln(P_m)^7$	$\ln(A_m)^8$	$u^*^9$	TCI <sup>10</sup>	$u^*:TCI$	$R^2$
Total	0.292 ***	0.048 ***	-0.037 ***	-0.334 ***	0.790 ***	-1.018 ***	0.278 ***
GD <sup>1</sup>	0.299 ***	0.016	-0.041 ***	-0.183 ***	-0.293 *	0.239	0.158 ***
GN <sup>2</sup>	0.370 ***	0.029	-0.023 ***	-0.386 ***	-0.038	0.081	0.103 ***
GT <sup>3</sup>	0.161	0.060 ***	-0.014 ***	-0.182	1.056 ***	-1.754	0.186 ***
DD <sup>4</sup>	0.393 ***	0.011	-0.020 ***	-0.154 *	0.306	-0.153	0.040 ***
DN <sup>5</sup>	0.661 ***	0.012	-0.026 ***	-0.443 ***	-0.035	0.399	0.088 ***
DT <sup>6</sup>	0.495 ***	0.017	-0.036 ***	-0.294 ***	0.564	-0.852	0.149 ***

497 <sup>1</sup> GD represents the growing season's daytime; <sup>2</sup> GN represents the growing season's nighttime;  
498 <sup>3</sup> GT represents the growing season's transition period; <sup>4</sup> DD represents the dormant season's  
499 daytime; <sup>5</sup> DN represents the dormant season's nighttime; <sup>6</sup> DT represents the dormant season's  
500 transition period. <sup>7</sup>  $A_m$ : maximum amplitude; <sup>8</sup>  $P_m$ : corresponding period of maximum amplitude. <sup>9</sup>  
501  $u^*$ : friction velocity; <sup>10</sup> TCI: terrain complexity index; \*\*\* represents  $P < 0.001$ ; \*\* represents  $P <$   
502 0.01; and \* represents  $P < 0.05$ .

503 To evaluate the impact of  $F_{s\_comb}$  on  $NEE_{obs}$  ( $F_c + F_s$ ), we further evaluated the  
504 slope (with intercept terms forced to zero) and NRMSE of  $F_c + F_{s\_comb}$  compared to  $F_c$   
505 +  $F_{s\_28}$ , as presented in Supplementary Materials Table 7 and Table 8. The  $F_{s\_28}$  in the  
506 three forest stands was underestimated by 28.6%–33.3% compared to the  $F_{s\_comb}$ , and  
507 the NRMSE of  $F_{s\_comb}$  versus the  $F_{s\_28}$  ranged from 59.2% to 67.2%. The  $NEE_{obs}$  with  
508  $F_{s\_28}$  was underestimated by 1.9%–4.3% compared to the  $NEE_{obs}$  with  $F_{s\_comb}$ . The  
509 NRMSE of  $NEE_{obs}$  with the  $F_{s\_comb}$  versus the  $F_{s\_28}$  in the three forest stands ranged  
510 from 16.0% to 25.4%. The analysis suggested that combining the  $F_s$  values based on  
511 different averaging [CO<sub>2</sub>] time windows in the decision-level fusion model could  
512 successfully weigh potential underestimation bias and random uncertainties.

513 The influences of  $F_s$  on the relationship between NEE observations and  
514 meteorological drivers, indicated the effect of uncertainty in  $F_s$  estimates on NEE  
515 observations. Our analysis showed that the correlations between NEE observations  
516 derived from  $F_c + F_s$  and both photosynthetic photon flux density (PPFD) and air  
517 temperature are lower compared to those obtained from  $F_c$  alone (Figure 1 and Figure  
518 2 in the Supplementary Materials). Additionally, the estimated light saturated net CO<sub>2</sub>  
519 assimilation ( $A_{max}$ ) is greater when NEE observations are estimated by  $F_s + F_c$ , as  
520 opposed to when NEE is estimated solely by  $F_c$ . This suggests that  $F_s$  significantly  
521 affects daytime NEE and can correct the estimation of  $A_{max}$  and related parameters. The  
522 relationship between NEE observations and PPFD is influenced by the size of averaging  
523 time window the  $F_s$  measurement. A larger averaging window results in less random  
524 uncertainty in the  $F_s$  estimation, thereby increasing the correlation between NEE



525 observations and meteorological drivers, including PPFD and  $T_a$ .

## 526 **4 Discussion**

### 527 4.1 Short-term $[CO_2]$ fluctuations above the forest canopy and $F_s$ estimates in complex 528 terrains

529 Compared to flat and uniform underlying surface, complex terrain and  
530 heterogeneous canopies modify the trajectory, speed distribution and direction of the  
531 airflow. Increased wind speeds and shifting wind directions also increase turbulent  
532 activity above the canopy, facilitating the mixing and dispersion of  $CO_2$ . This study  
533 found that short-term fluctuations of  $[CO_2]$  above the canopy exhibited a range of 1 to  
534 10 min (Fig. 2). These fluctuations were characterized by an average  $P_m$  ranging from  
535 2.313 to 2.784 min (Table 2). Our results are in line with previous research using  
536 wavelet analysis, which reported fluctuation periods of  $[CO_2]$  within and above the  
537 forest canopy to be between 14 and 116 s (Cava et al., 2004). Their observations of the  
538 canopy waves during periods of extreme atmospheric stability (when  $z/L \gg 1$ ) exhibited  
539 a dominant period of 1–2 min, consistent with our findings. The period of  $[CO_2]$   
540 fluctuations was found to be predominantly influenced by turbulent fluxes and the  
541 residence time of  $CO_2$  within the canopy. This indicated a potential correlation between  
542  $P_m$  and the residence time of  $CO_2$  within the canopy. Fuentes et al. (2006) employed a  
543 Lagrangian model and calculated the residence time of air parcels released near the  
544 ground and canopy, finding values ranging from 3 to 10 min and from 1 to 10 min,  
545 respectively. Similarly, Edburg et al. (2011) used the standard deviation of  $[CO_2]$

546 averages to determine CO<sub>2</sub> residence time at different locations, including the ground,  
547 within the canopy, and in their gas mixtures, yielding values of 8.6, 3.6, and 5.6 min,  
548 respectively. The results of these simulation experiments are consistent with our study,  
549 further supporting the association between [CO<sub>2</sub>] fluctuations above the forest canopy  
550 and CO<sub>2</sub> residence time.

551 Tree density and canopy structure also play a role in influencing the air parcel  
552 residence time; in flat terrains, the air parcel residence time correlate with  $u^*$  (Gerken  
553 et al., 2017), and an increase in vegetation leaf area leads to longer residence times  
554 when turbulence is not fully penetrative. During the growing season, forests exhibit  
555 higher leaf area index and canopy densities compared to the dormant season, resulting  
556 in longer  $P_m$  of short-term [CO<sub>2</sub>] fluctuations above the canopy (Fig. 3). Additionally,  
557 at night, stable atmospheric conditions lead to longer residence times due to suppressed  
558 turbulent mixing, resulting in relatively long nighttime  $P_m$  values compared to daytime  
559 and transition periods (Fig. 3).

560 Complex terrains introduce complex changes in air flow structures, including  
561 gravity-induced waves, drainage, and nonlinear waves induced by single gusts, leading  
562 to dramatic [CO<sub>2</sub>] fluctuations. These dynamics contribute to uncertainties in estimating  
563  $F_s$ . During nighttime, long-wave radiation emitted from the valley soil surface leads to  
564 the cooling and downslope acceleration of air near the soil surface due to gravity,  
565 potentially causing katabatic flow. As inertia-driven upslope winds are halted by  
566 katabatic acceleration, a local shallow drainage flow is established, reaching a quasi-  
567 equilibrium state approximately 1.5 h after sunset (Nadeau et al., 2013). Under stable

568 atmospheric conditions, even gentle slopes (around  $1^\circ$ ) can generate strong gravity-  
569 driven waves (Belušić and Mahrt, 2012). Consequently, advection may complicate the  
570 interpretation of nighttime EC measurements at certain relatively gentle sites, but this  
571 complexity is not evident during daytime measurements (Leuning et al., 2008).  
572 Advection plays a role in depleting the  $\text{CO}_2$  accumulated within the canopy, resulting  
573 in lower  $F_s$  fluxes and establishing an inverse relationship between storage and  
574 advection (Van Gorsel et al., 2011). The occurrence of larger  $F_s$  values for long  $P_m$   
575 values suggests weaker advection compared to short  $P_m$  values (Fig. 4). In our study,  
576 we observed that the  $F_s$  magnitude was relatively large during nighttime and transition  
577 periods, while it was smaller during daytime (Fig. 4), which is consistent with the  
578 findings reported by Wang et al. (2016).

579         The terrain complexity and the diversity within the canopy significantly affect the  
580 airflow separation in the atmospheric boundary layer. This results in weakened air  
581 circulation within the canopy and spatial variation in the patterns and extent of airflow  
582 separation (Grant et al., 2015). During nighttime and transition periods in a closed  
583 canopy, the turbulent coupling state above and below the canopy gradually decouples,  
584 eventually reaching complete decoupling as the  $u^*$  decreases (Fig. 5). However, this  
585 decoupling does not lead to stable stratification within the canopy. Despite the  
586 occurrence of decoupling and advection in the closed canopy, waves are unlikely to  
587 exist within the canopy itself (Van Gorsel et al., 2011). As a result, a consistent trend  
588 in the variation of  $F_s$  with  $\tau$  is observed across the three forest stands during the growing  
589 season, independent of  $P_m$  (Fig. 9). Conversely, in an open canopy where waves are

590 present, the observations of  $F_s$  become more complex. This complexity could be the  
591 primary reason why the variation of  $F_s$  with  $[CO_2]$  averaging time windows differs  
592 between the three forest stands for short  $P_m$  values during the dormant season daytime  
593 (Fig. 9). The presence of waves introduces additional variability in the measurements,  
594 leading to differences in  $F_s$  estimates based on different  $[CO_2]$  averaging time windows  
595 in these particular conditions.

#### 596 4.2 Uncertainty in forest ecosystem $F_s$ measurement in complex terrains

597 The random uncertainty of  $F_s$  shares similarities with NEE estimation. For  
598 example, the magnitude of  $F_s$  measurements is positively correlated with the standard  
599 deviation of random uncertainty in  $F_s$ . Additionally, the overall distribution of  $F_s$   
600 measurements exhibits a non-Gaussian distribution with a high peak, aligning with the  
601 statistical properties of NEE uncertainty (Richardson et al., 2006; Richardson et al.,  
602 2008). The uncertainty in the storage term depends a lot on the set-up used, together  
603 with the biological activity of the ecosystem, and the height of the control volume. In  
604 addition, various factors contribute to the uncertainty in  $F_s$  estimates, including flux  
605 measurement footprint variations, sampling frequency, spatial sampling resolution of  
606  $CO_2/H_2O$  concentrations, and instrumental measurement accuracy. The uncertainty  
607 arising from variations in the flux measurement footprint is considerable, typically on  
608 the order of tens of percentages, which is an order of magnitude higher than typical  
609 sensor errors (Metzger, 2018). The AP200 atmospheric profiling system used in this  
610 study has an accuracy of  $\pm 0.5 \mu mol mol^{-1}$  and  $\pm 0.1 mmol mol^{-1}$  for  $CO_2$  and  $H_2O$   
611 concentration measurements, respectively (Montagnani et al., 2018). The AP200 adopts

612 buffer volumes to mix the gas. Efforts to reduce random errors in [CO<sub>2</sub>] originating  
613 from pressure fluctuations include adding buffer volumes before IRGA pumping tests  
614 (Marcolla et al., 2014). The buffer volumes are fully mixed during gas extraction and  
615 performs a weighted average of [CO<sub>2</sub>] instantaneous measurements to minimize the  
616 sampling error for each level's [CO<sub>2</sub>] measurement (Cescatti et al., 2016).

617 The  $F_s$  estimates can be influenced by singular eddies that penetrate inside the  
618 canopy (Finnigan, 2006). Accurate calculation of  $F_s$  requires considering the period of  
619 [CO<sub>2</sub>] fluctuations with the eddy coherence structure. The spectral energy of the  $F_s$  time  
620 series is primarily concentrated between 0.001 and 0.2 Hz (500 and 5 s, respectively).  
621 However, even with sampling frequencies of 2 Hz and below, significantly lower  $F_s$   
622 values are obtained (Bjorkegren et al., 2015). The Nyquist-Shannon sampling theorem  
623 dictates that accurate measurements of [CO<sub>2</sub>] require a sampling period no longer than  
624 half the period of [CO<sub>2</sub>] fluctuations. Consequently, to monitor short-term changes in  
625 [CO<sub>2</sub>], measurements must be taken over a period no longer than half of the period  
626 corresponding to the maximum amplitude (or major energy) of [CO<sub>2</sub>] fluctuations. In  
627 this study, the average  $P_m$  for [CO<sub>2</sub>] fluctuations fell within the range of 2.313–2.784  
628 min (Table 2). Therefore, it is crucial to ensure that the sampling period for [CO<sub>2</sub>] does  
629 not exceed 1.256 to 1.392 min, which corresponds to half the average  $P_m$  range.  
630 Monitoring fluctuations of  $P_m$  for less than 4 min during a 2-min monitoring period of  
631 [CO<sub>2</sub>] presents a significant challenge. This is a primary reason that the systematic bias  
632 and random error in  $F_s$  estimate with a single profile system are irreconcilable (Wang  
633 et al., 2016). Short-term [CO<sub>2</sub>] fluctuations are mainly influenced by boundary layer

634 turbulence, and sampling errors in incomplete fluctuation cycles will be superimposed  
635 with the real advection flux (anisotropy) dispersion in complex terrains (Van Gorsel et  
636 al., 2011). This substantially increases the random uncertainty in  $F_s$  based on shorter  
637  $[CO_2]$  averaging time windows (Fig. 6 and Fig. 8). As a result, the deviation of NEE  
638 estimates from the actual value expands.

639       Fluxes in heterogeneous regions are significantly higher than in uniform regions.  
640 The energy transfer from the ground surface to large eddies occurs primarily in areas  
641 with pronounced heterogeneity, and this energy distribution is uneven across the region  
642 (Aubinet et al., 2012). Once large-scale eddies acquire energy, their cascading of energy  
643 to smaller-scale eddies is influenced by topographic features, leading to variations in  
644 these smaller-scale eddies along different flow streams (Chen et al., 2023). In complex  
645 terrains, the bidirectional airflow within forests along slopes can cause the decoupling  
646 of soil  $CO_2$  fluxes from EC measurements above the forest canopy (Feigenwinter et al.,  
647 2008; Aubinet et al., 2003), leading to significant errors in  $CO_2$  flux measurements.  
648 Forest soil serves as the primary source of  $CO_2$  gas and regions of high flux over  
649 complex terrains act like chimneys, transporting air parcels from the soil surface within  
650 forests (Chen et al., 2019). By increasing the number of gas concentration sampling  
651 points near the ground, the horizontal representativeness can be enhanced, thereby  
652 reducing the bias in the estimation of  $F_s$  (Nicolini et al., 2018). In situations where  
653 turbulence is not well-developed, and  $CO_2$  mixing is inadequate, the trend of  $F_s$  with  
654 turbulence intensity aligns with that of advective fluxes, which is opposite to that of  
655 turbulent fluxes (Mchugh et al., 2017). The temporal dynamics and amplitudes of  $F_s$

656 changes are influenced by topography complexity and wind conditions above the forest  
657 canopy (Fig. 10). Locations with more complex and sloping topography at the flux  
658 tower are more likely to generate advective fluxes that may not be easily observed at a  
659 single point.

660 Estimating landscape CO<sub>2</sub> fluxes in complex terrains solely based on  
661 measurements from a single flux tower can introduce significant errors and biases that  
662 are not acceptable. The magnitude of these errors in F<sub>s</sub> estimates is dependent on the  
663 height of the forest canopy and the endogenous source/sink (Chen et al., 2020). To  
664 mitigate errors and biases associated with estimating F<sub>s</sub> in complex terrains, we  
665 employed a regression modeling approach using the decision-level fusion model. This  
666 method involves computing a weighted average of F<sub>s</sub> based on different [CO<sub>2</sub>]  
667 averaging time windows, effectively reducing errors and biases in the estimation of F<sub>s</sub>  
668 (see Table 5). In fact, from the definition of storage flux, it can be seen that weighting  
669 the storage flux is essentially weighting the [CO<sub>2</sub>] in the average time window, which  
670 means replacing spatial sequences with temporal sequences for weighting. The  
671 weighting coefficients used to construct the model were based on the relative errors and  
672 biases of F<sub>s</sub> estimation, with the weighting coefficient decreasing as the represented  
673 moment's length increased. To obtain more accurate estimates of forest ecosystem F<sub>s</sub> in  
674 complex terrains, further research should focus on understanding the spatiotemporal  
675 patterns and dynamics of [CO<sub>2</sub>].

## 676 **5 Conclusions**

677 This study investigated the impact of short-term [CO<sub>2</sub>] fluctuations on the  
678 estimation of F<sub>s</sub> in temperate forest ecosystems within complex terrains. Additionally,  
679 it examined the F<sub>s</sub> uncertainty and the contribution of the F<sub>s</sub> to NEE using data from  
680 three flux towers. To enhance F<sub>s</sub> uncertainty estimation, statistical sampling techniques  
681 were applied based on the individual tower approach.

682 The results highlighted the significance of considering multiple time windows for  
683 averaging [CO<sub>2</sub>] when estimating F<sub>s</sub>, as [CO<sub>2</sub>] above the forest canopies exhibited  
684 fluctuations with periods ranging from 1 to 10 minutes. Diurnal, seasonal, and spatial  
685 variations were observed in the amplitude and periodicity of [CO<sub>2</sub>] fluctuations,  
686 highlighting the need for thoughtful sampling strategies. The use of individual gas  
687 analyzers to sample the CO<sub>2</sub> in the control volume was inadequate, leading to  
688 systematic biases and random errors in the F<sub>s</sub> estimates. Increasing [CO<sub>2</sub>] averaging  
689 time windows mitigated the effect of [CO<sub>2</sub>] fluctuations on F<sub>s</sub> estimates, reducing both  
690 their magnitude and uncertainty.

691 The study also revealed that the uncertainty of F<sub>s</sub> followed a non-normal  
692 distribution, with its standard deviation positively correlated with F<sub>s</sub> magnitude, which  
693 has important implications for quality control. To improve F<sub>s</sub> estimation, a decision-  
694 level fusion model was introduced, integrating F<sub>s</sub> estimates from multiple [CO<sub>2</sub>]  
695 averaging time windows, effectively reducing the impact of short-term [CO<sub>2</sub>]  
696 fluctuations while considering underestimation bias and random errors. The  
697 contribution of F<sub>s</sub> to NEE exhibited diurnal, seasonal, and spatial variations associated



698 with  $u^*$ , contributing to the NEE observations at rates ranging from 17.2% to 82.0%  
699 depending on the turbulent mixing and terrain complexity. The influence of terrain  
700 complexity on the relationship between  $[\text{CO}_2]$  fluctuations, turbulent mixing, and the  
701 contribution of  $F_s$  to NEE was also evident. The findings from the three flux towers  
702 allowed for the generalization of these results beyond the study site. These insights  
703 provide crucial scientific support for the practical application of the eddy covariance  
704 technique and advance our understanding of accurately estimating NEE in forest  
705 ecosystems in complex terrains.

## 706 **Appendix A**

### 707 *A.1 the weight parameters of the decision-level fusion model*

708 For each 30-min  $\text{CO}_2$  storage flux ( $F_s$ ) estimate based on the  $\text{CO}_2$  concentration  
709 ( $[\text{CO}_2]$ ) averaging time window ( $\tau$ ), the weight in the decision-level fusion model can  
710 be obtained by weighting the random uncertainty and bias of  $F_{s_\tau}$ .

711 The weight of the random uncertainty for the  $F_{s_\tau}$  is expressed as follows:

$$w_\tau = \frac{1/\sigma(\varepsilon_\tau)}{\sum_j 1/\sigma(\varepsilon_j)}, \quad (\text{A.1})$$

712 where  $\sigma(\varepsilon_\tau)$  is the random uncertainty of the  $F_{s_\tau}$ , qualified as the standard deviation.

713 The weight of the bias for the  $F_{s_\tau}$  is expressed as follows:

$$W_\tau = \frac{K_\tau}{\sum_j K_j}, \quad (\text{A.2})$$

714 where  $K_\tau$  is the slope between the  $F_{s_\tau}$  and  $F_{s_{28}}$ .

715 Ultimately, the weight of the  $F_{s_\tau}$  in the decision-level fusion model can be  
716 calculated using the following equation:

$$w_{\tau}^* = rw_{\tau} + (1 - r)W_{\tau}, \quad (\text{A.3})$$

717 where  $r$  represents the proportion of the weight of random uncertainty.

## 718 A.2 Complex terrain index

719 This study employed a novel descriptor called the terrain complexity index (*TCI*)

720 to quantify the complexity of the three-dimensional terrain. For a given unit area, the

721 *TCI* equation can be expressed as follows:

$$TCI = (1 - P_d \cos \alpha_d)(1 - Z_d^{-1})(D_f - 2)^{-H/\ln(12)}, \quad (\text{A.4})$$

722 where,  $P_d$  represents the volume of terrain above the lowest elevation of an area

723 unit ( $V_u$ ) divided by the product of its largest vertically projected area ( $S_v$ ) and the

724 edge length of the side of the area unit ( $d$ ), expressed as  $P_d = V_u/(S_v d)$ ;  $P_d$  was

725 defined to be one when the  $S_v$  is zero. Given  $V_u$ , an increase in  $S_v$  correlates with a

726 higher degree of terrain complexity. Notably, the  $P_d$  is defined as 1 when the terrain

727 volume is 0 or when the terrain surface of the area unit was parallel to the horizontal

728 plane and was smooth and homogeneous.  $\alpha_d$  indicates the slope of the area unit.  $Z_d$

729 denoted the terrain roughness, which defined as the ratio of the terrain surface area to

730 the projected horizontal plane (Loke and Chisholm, 2022). The value of  $Z_d$  is in the

731 range of  $[1, +\infty)$ . The larger  $Z_d$ , the more complex the terrain.  $D_f$  is the fractal

732 dimension of terrain surface area, which ranged from 2 to 3 and described the

733 complexity in spatially self-similar structure of the local surface within the area unit

734 and the area unit surface (B. B. Mandelbrot, 1967; Taud and Parrot, 2005). Employing

735 terrain surface area, the box-counting method is used to estimate fractal dimension of

736 unit area.  $H$  represented the Shannon-Wiener index and expressed as  $H =$

737  $-\sum_{i=1}^n P_i \ln(P_i)$ , capturing the uniformity of the spatial distribution of the pixel  
 738 aspects within the area unit (Brown, 1997). When the aspect of each pixel is divided  
 739 into  $30^\circ$  segments,  $P_i$  denotes the proportion of the  $i^{\text{th}}$  type of pixel aspects within the  
 740 area unit and  $n$  was the total number of pixel aspect types within the area unit. A  
 741 larger  $H$  indicates a more complex terrain. When the number of pixel aspect types in  
 742 the area unit is kept constant, it's essential to recognize that greater uniformity in the  
 743 distribution of all pixel aspect in the area unit results in a larger  $H$ . Similarly, when the  
 744 uniformity of the distribution of pixel aspects in the area unit is kept constant, a larger  
 745  $H$  is achieved with an increase in the observation of the number of pixel aspect types.

746 To quantify the terrain complexity of the underlying surface around the flux towers,  
 747 we computed the quartiles of  $TCI$  for all area units within a sector (divided by  $30^\circ$ ) with  
 748 a radius of 380 m. A weighted geometric mean was employed to construct  $TCIs$ , which  
 749 describe the statistical distribution of  $TCI$  of the sector. The  $TCIs$  represents the  
 750 topographic complexity of the sector and are calculated using the following equation:

$$751 \quad TCI_s = (TCI_5 TCI_{25} TCI_{50} TCI_{75} TCI_{95})^{1/5} \quad (A.5)$$

752 where  $TCI_5$ ,  $TCI_{25}$ ,  $TCI_{50}$ ,  $TCI_{75}$ , and  $TCI_{95}$  are the quartiles of 5%, 25%, 50%, 75%,  
 753 and 95%, respectively. The  $TCIs$  values range from 0 to 1, with higher values indicating  
 754 greater terrain complexity.

755 *Data availability.* Data used in this paper are available at the Science Data Bank  
 756 (<https://www.scidb.cn/en/s/7ZfQZv>) or upon request to the corresponding author.

757 *Author contributions.* DT developed the manuscript; JZ was responsible for  
 758 conceptualizing the idea and designing the research study; TG substantially structured

759 the manuscript; FY contributed to the data collection process; YZ helped in the design  
760 and preparation of the figures and tables; XZ and BY revised the manuscript.

761 *Competing interests.* The authors declare that they have no known competing  
762 financial interests or personal relationships that could have appeared to influence the  
763 work reported in this paper.

764 *Acknowledgments.* We are grateful to Qingyuan Forest CERN, Chinese Academy of  
765 Sciences/Qingyuan Forest, National Observation and Research Station, Liaoning  
766 Province, China for providing forest sites, instrument systems, and logistic supports.

767 *Financial support.* This research was financially supported by the National Natural  
768 Science Foundation of China (No. 32192435), the China Postdoctoral Science  
769 Foundation (No. 2023M733672), Key R&D Program of Liaoning Province  
770 (2023JH2/101800043), and the Postdoctoral Research Startup Foundation of Liaoning  
771 Province of China (No. 2022-BS-022).

## 772 **Reference**

773 Aubinet, M., Heinesch, B., and Yernaux, M.: Horizontal and Vertical CO<sub>2</sub> Advection In A Sloping Forest,  
774 Boundary-Layer Meteorology, 108, 397-417, 10.1023/a:1024168428135, 2003.

775 Aubinet, M., Vesala, T., and Papale, D.: Eddy Covariance: A Practical Guide to Measurement and Data  
776 Analysis, Springer Atmospheric Sciences, Springer, Dordrecht, XXII, 438 pp., 10.1007/978-94-007-  
777 2351-1, 2012.

778 Aubinet, M., Grelle, A., Ibrom, A., Rannik, Ü., Moncrieff, J., Foken, T., Kowalski, A. S., Martin, P. H.,  
779 Berbigier, P., Bernhofer, C., Clement, R., Elbers, J., Granier, A., Grünwald, T., Morgenstern, K.,  
780 Pilegaard, K., Rebmann, C., Snijders, W., Valentini, R., and Vesala, T.: Estimates of the Annual Net  
781 Carbon and Water Exchange of Forests: The EUROFLUX Methodology, in: Advances in Ecological  
782 Research Volume 30, Advances in Ecological Research, 113-175, 10.1016/s0065-2504(08)60018-5,  
783 2000.

784 B. B. Mandelbrot: How Long Is the Coast of Britain? Statistical Self-Similarity and Fractional Dimension,  
785 Science, 156, 636-638, 1967.

786 Belušić, D. and Mahrt, L.: Is geometry more universal than physics in atmospheric boundary layer flow?,  
787 Journal of Geophysical Research: Atmospheres, 117, n/a-n/a, 10.1029/2011jd016987, 2012.

788 Bjorkegren, A. B., Grimmond, C. S. B., Kotthaus, S., and Malamud, B. D.: CO<sub>2</sub> emission estimation in

789 the urban environment: Measurement of the CO<sub>2</sub> storage term, *Atmospheric Environment*, 122, 775-790,  
790 10.1016/j.atmosenv.2015.10.012, 2015.

791 Brown, S.: Estimating Biomass and Biomass Change of Tropical Forests: A Primer, *FAO Forestry Paper*,  
792 134, 1997.

793 Cava, D., Giostra, U., Siqueira, M., and Katul, G.: Organised motion and radiative perturbations in the  
794 nocturnal canopy sublayer above an even-aged pine forest, *Boundary-Layer Meteorology*, 112, 129-157,  
795 DOI 10.1023/B:BOUN.0000020160.28184.a0, 2004.

796 Cescatti, A., Marcolla, B., Goded, I., and Gruening, C.: Optimal use of buffer volumes for the  
797 measurement of atmospheric gas concentration in multi-point systems, *Atmospheric Measurement*  
798 *Techniques*, 9, 4665-4672, 10.5194/amt-9-4665-2016, 2016.

799 Chen, B., Chamecki, M., and Katul, G. G.: Effects of topography on in-canopy transport of gases emitted  
800 within dense forests, *Quarterly Journal of the Royal Meteorological Society*, 145, 2101-2114,  
801 10.1002/qj.3546, 2019.

802 Chen, B. C., Chamecki, M., and Katul, G. G.: Effects of Gentle Topography on Forest-Atmosphere Gas  
803 Exchanges and Implications for Eddy-Covariance Measurements, *J Geophys Res-Atmos*, 125, ARTN  
804 e2020JD032581  
805 10.1029/2020JD032581, 2020.

806 Chen, J., Chen, X., Jia, W., Yu, Y., and Zhao, S.: Multi-sites observation of large-scale eddy in surface  
807 layer of Loess Plateau, *Science China Earth Sciences*, 66, 871–881, [https://doi.org/10.1007/s11430-022-](https://doi.org/10.1007/s11430-022-1035-4)  
808 [1035-4](https://doi.org/10.1007/s11430-022-1035-4), 2023.

809 de Araújo, A. C., J.P.H.B., O., Dolman, A. J., B., K., M.J., W., and J.R., E.: Implications of CO<sub>2</sub> pooling  
810 on delta C13 of ecosystem respiration and leaves in Amazonian forest, *Biogeosciences*, 5, 779-795,  
811 10.5194/bg-5-779-2008, 2008.

812 de Araújo, A. C., Dolman, A. J., Waterloo, M. J., Gash, J. H. C., Kruijt, B., Zanchi, F. B., de Lange, J. M.  
813 E., Stoevelaar, R., Manzi, A. O., Nobre, A. D., Lootens, R. N., and Backer, J.: The spatial variability of  
814 CO<sub>2</sub> storage and the interpretation of eddy covariance fluxes in central Amazonia, *Agricultural and Forest*  
815 *Meteorology*, 150, 226-237, 10.1016/j.agrformet.2009.11.005, 2010.

816 Edburg, S. L., Stock, D., Lamb, B. K., and Patton, E. G.: The Effect of the Vertical Source Distribution  
817 on Scalar Statistics within and above a Forest Canopy, *Boundary-Layer Meteorology*, 142, 365-382,  
818 10.1007/s10546-011-9686-1, 2011.

819 Feigenwinter, C., Bernhofer, C., and Vogt, R.: The Influence of Advection on the Short Term CO<sub>2</sub>-Budget  
820 in and Above a Forest Canopy, *Boundary-Layer Meteorology*, 113, 201-224,  
821 10.1023/B:BOUN.0000039372.86053.ff, 2004.

822 Feigenwinter, C., Bernhofer, C., Eichelmann, U., Heinesch, B., Hertel, M., Janous, D., Kolle, O.,  
823 Lagergren, F., Lindroth, A., Minerbi, S., Moderow, U., Mölder, M., Montagnani, L., Queck, R., Rebmann,  
824 C., Vestin, P., Yernaux, M., Zeri, M., Ziegler, W., and Aubinet, M.: Comparison of horizontal and vertical  
825 advective CO<sub>2</sub> fluxes at three forest sites, *Agricultural and Forest Meteorology*, 148, 12-24,  
826 10.1016/j.agrformet.2007.08.013, 2008.

827 Finnigan, J.: The storage term in eddy flux calculations, *Agricultural and Forest Meteorology*, 136, 108-  
828 113, 10.1016/j.agrformet.2004.12.010, 2006.

829 Finnigan, J., Ayotte, K., Harman, I., Katul, G., Oldroyd, H., Patton, E., Poggi, D., Ross, A., and Taylor,  
830 P.: Boundary-Layer Flow Over Complex Topography, *Boundary-Layer Meteorology*, 177, 247-313,  
831 10.1007/s10546-020-00564-3, 2020.

832 Fuentes, J. D., Wang, D., Bowling, D. R., Potosnak, M., Monson, R. K., Goliff, W. S., and Stockwell, W.

833 R.: Biogenic Hydrocarbon Chemistry within and Above a Mixed Deciduous Forest, *Journal of*  
834 *Atmospheric Chemistry*, 56, 165-185, 10.1007/s10874-006-9048-4, 2006.

835 Gao, T., Yu, L.-Z., Yu, F.-Y., Wang, X.-C., Yang, K., Lu, D.-L., Li, X.-F., Yan, Q.-L., Sun, Y.-R., Liu, L.-  
836 F., Xu, S., Zhen, X.-J., Ni, Z.-D., Zhang, J.-X., Wang, G.-F., Wei, X.-H., Zhou, X.-H., and Zhu, J.-J.:  
837 Functions and applications of Multi-Tower Platform of Qingyuan Forest Ecosystem Research Station of  
838 Chinese Academy of Sciences, *Chinese journal of applied ecology*, 31, 695-705, 10.13287/j.1001-  
839 9332.202003.040, 2020.

840 Gerken, T., Chamecki, M., and Fuentes, J. D.: Air-Parcel Residence Times Within Forest Canopies,  
841 *Boundary-Layer Meteorology*, 165, 29-54, 10.1007/s10546-017-0269-7, 2017.

842 Grant, E. R., Ross, A. N., Gardiner, B. A., and Mobbs, S. D.: Field Observations of Canopy Flows over  
843 Complex Terrain, *Boundary-Layer Meteorology*, 156, 231-251, 10.1007/s10546-015-0015-y, 2015.

844 Gu, L., Massman, W. J., Leuning, R., Pallardy, S. G., Meyers, T., Hanson, P. J., Riggs, J. S., Hosman, K.  
845 P., and Yang, B.: The fundamental equation of eddy covariance and its application in flux measurements,  
846 *Agricultural and Forest Meteorology*, 152, 135-148, 10.1016/j.agrformet.2011.09.014, 2012.

847 Heinesch, B., Yernaux, M., and Aubinet, M.: Some methodological questions concerning advection  
848 measurements: a case study, *Boundary-Layer Meteorology*, 122, 457-478, 10.1007/s10546-006-9102-4,  
849 2007.

850 Hollinger, D. Y. and Richardson, A. D.: Uncertainty in eddy covariance measurements and its application  
851 to physiological models, *Tree Physiol*, 25, 873-885, DOI 10.1093/treephys/25.7.873, 2005.

852 Huang, N. E., Shen, Z., Long, S. R., Wu, M. C., Shih, H. H., Zheng, Q., Yen, N.-C., Tung, C. C., and Liu,  
853 H. H.: The empirical mode decomposition and the Hilbert spectrum for nonlinear and non-stationary  
854 time series analysis, *Proceedings of the Royal Society of London. Series A: Mathematical, Physical and*  
855 *Engineering Sciences*, 454, 903-995, 10.1098/rspa.1998.0193, 1998.

856 Khélifa, N., Lecollinet, M., and Himbert, M.: Molar mass of dry air in mass metrology, *Measurement*,  
857 40, 779-784, 10.1016/j.measurement.2006.05.009, 2007.

858 Leuning, R., Zegelin, S. J., Jones, K., Keith, H., and Hughes, D.: Measurement of horizontal and vertical  
859 advection of CO<sub>2</sub> within a forest canopy, *Agricultural and Forest Meteorology*, 148, 1777-1797,  
860 10.1016/j.agrformet.2008.06.006, 2008.

861 Li, S., Yan, Q., Liu, Z., Wang, X., Yu, F., Teng, D., Sun, Y., Lu, D., Zhang, J., Gao, T., and Zhu, J.:  
862 Seasonality of albedo and fraction of absorbed photosynthetically active radiation in the temperate  
863 secondary forest ecosystem: A comprehensive observation using Qingyuan Ker towers, *Agricultural and*  
864 *Forest Meteorology*, 333, 10.1016/j.agrformet.2023.109418, 2023.

865 Li, Y.-C., Liu, F., Wang, C.-K., Gao, T., and Wang, X.-C.: Carbon budget estimation based on different  
866 methods of CO<sub>2</sub> storage flux in forest ecosystems, *Chinese journal of applied ecology*, 31, 3665-3673,  
867 10.13287/j.1001-9332.202011.004, 2020.

868 Loke, L. H. L. and Chisholm, R. A.: Measuring habitat complexity and spatial heterogeneity in ecology,  
869 *Ecology Letters*, 25, 2269-2288, 10.1111/ele.14084, 2022.

870 Marcolla, B., Cobbe, I., Minerbi, S., Montagnani, L., and Cescatti, A.: Methods and uncertainties in the  
871 experimental assessment of horizontal advection, *Agricultural and Forest Meteorology*, 198-199, 62-71,  
872 10.1016/j.agrformet.2014.08.002, 2014.

873 McHugh, I. D., Beringer, J., Cunningham, S. C., Baker, P. J., Cavagnaro, T. R., Mac Nally, R., and  
874 Thompson, R. M.: Interactions between nocturnal turbulent flux, storage and advection at an "ideal"  
875 eucalypt woodland site, *Biogeosciences*, 14, 3027-3050, 10.5194/bg-14-3027-2017, 2017.

876 McMaster, G. S. and Wilhelm, W. W.: Growing degree-days: one equation, two interpretations,

877 Agricultural and Forest Meteorology, 87, 291-300, Doi 10.1016/S0168-1923(97)00027-0, 1997.

878 Metzger, S.: Surface-atmosphere exchange in a box: Making the control volume a suitable representation  
879 for in-situ observations, Agricultural and Forest Meteorology, 255, 68-80,  
880 10.1016/j.agrformet.2017.08.037, 2018.

881 Montagnani, L., Grunwald, T., Kowalski, A., Mammarella, I., Merbold, L., Metzger, S., Sedlak, P., and  
882 Siebicke, L.: Estimating the storage term in eddy covariance measurements: the ICOS methodology, Int  
883 Agrophys, 32, 551-567, 10.1515/intag-2017-0037, 2018.

884 Montagnani, L., Manca, G., Canepa, E., Georgieva, E., Acosta, M., Feigenwinter, C., Janous, D.,  
885 Kerschbaumer, G., Lindroth, A., Minach, L., Minerbi, S., Mölder, M., Pavelka, M., Seufert, G., Zeri, M.,  
886 and Ziegler, W.: A new mass conservation approach to the study of CO<sub>2</sub> advection in an alpine forest,  
887 Journal of Geophysical Research, 114, 10.1029/2008jd010650, 2009.

888 Nadeau, D. F., Pardyjak, E. R., Higgins, C. W., Huwald, H., and Parlange, M. B.: Flow during the evening  
889 transition over steep Alpine slopes, Quarterly Journal of the Royal Meteorological Society, 139, 607-624,  
890 10.1002/qj.1985, 2013.

891 Nicolini, G., Aubinet, M., Feigenwinter, C., Heinesch, B., Lindroth, A., Mamadou, O., Moderow, U.,  
892 Mölder, M., Montagnani, L., Rebmann, C., and Papale, D.: Impact of CO<sub>2</sub> storage flux sampling  
893 uncertainty on net ecosystem exchange measured by eddy covariance, Agricultural and Forest  
894 Meteorology, 248, 228-239, 10.1016/j.agrformet.2017.09.025, 2018.

895 Richardson, A. D., Hollinger, D. Y., Burba, G. G., Davis, K. J., Flanagan, L. B., Katul, G. G., William  
896 Munger, J., Ricciuto, D. M., Stoy, P. C., Suyker, A. E., Verma, S. B., and Wofsy, S. C.: A multi-site  
897 analysis of random error in tower-based measurements of carbon and energy fluxes, Agricultural and  
898 Forest Meteorology, 136, 1-18, 10.1016/j.agrformet.2006.01.007, 2006.

899 Richardson, A. D., Mahecha, M. D., Falge, E., Kattge, J., Moffat, A. M., Papale, D., Reichstein, M.,  
900 Stauch, V. J., Braswell, B. H., Churkina, G., Kruijt, B., and Hollinger, D. Y.: Statistical properties of  
901 random CO<sub>2</sub> flux measurement uncertainty inferred from model residuals, Agricultural and Forest  
902 Meteorology, 148, 38-50, 10.1016/j.agrformet.2007.09.001, 2008.

903 Sha, J., Zou, J., and Sun, J.: Observational study of land-atmosphere turbulent flux exchange over  
904 complex underlying surfaces in urban and suburban areas, SCIENCE CHINA-EARTH SCIENCES, 64,  
905 1050-1064, 10.1007/s11430-020-9783-2, 2021.

906 Siebicke, L., Steinfeld, G., and Foken, T.: CO<sub>2</sub>-gradient measurements using a parallel multi-analyzer  
907 setup, Atmospheric Measurement Techniques, 4, 409-423, 10.5194/amt-4-409-2011, 2011.

908 Taud, H. and Parrot, J.-F.: Measurement of DEM roughness using the local fractal dimension,  
909 Géomorphologie : relief, processus, environnement, 11, 327-338, 10.4000/geomorphologie.622, 2005.

910 van Gorsel, E., Harman, I. N., Finnigan, J. J., and Leuning, R.: Decoupling of air flow above and in plant  
911 canopies and gravity waves affect micrometeorological estimates of net scalar exchange, Agricultural  
912 and Forest Meteorology, 151, 927-933, 10.1016/j.agrformet.2011.02.012, 2011.

913 Wang, J., Shi, T., Yu, D., Teng, D., Ge, X., Zhang, Z., Yang, X., Wang, H., and Wu, G.: Ensemble  
914 machine-learning-based framework for estimating total nitrogen concentration in water using drone-  
915 borne hyperspectral imagery of emergent plants: A case study in an arid oasis, NW China, Environmental  
916 Pollution, 266, 10.1016/j.envpol.2020.115412, 2020.

917 Wang, X., Wang, C., Guo, Q., and Wang, J.: Improving the CO<sub>2</sub> storage measurements with a single  
918 profile system in a tall-dense-canopy temperate forest, Agricultural and Forest Meteorology, 228-229,  
919 327-338, 10.1016/j.agrformet.2016.07.020, 2016.

920 Warton, D. I., Duursma, R. A., Falster, D. S., and Taskinen, S.: smatr 3- an R package for estimation and

921 inference about allometric lines, *Methods in Ecology and Evolution*, 3, 257-259, 10.1111/j.2041-  
922 210X.2011.00153.x, 2012.

923 Webb, E. K., Pearman, G. I., and Leuning, R.: Correction of flux measurements for density effects due  
924 to heat and water vapour transfer, *Quarterly Journal of the Royal Meteorological Society*, 106, 85-100,  
925 10.1002/qj.49710644707, 1980.

926 Xu, K., Pingingtha-Durden, N., Luo, H., Durden, D., Sturtevant, C., Desai, A. R., Florian, C., and Metzger,  
927 S.: The eddy-covariance storage term in air: Consistent community resources improve flux measurement  
928 reliability, *Agricultural and Forest Meteorology*, 279, 10.1016/j.agrformet.2019.107734, 2019.

929 Yang, B., Hanson, P. J., Riggs, J. S., Pallardy, S. G., Heuer, M., Hosman, K. P., Meyers, T. P., Wullschleger,  
930 S. D., and Gu, L.-H.: Biases of CO<sub>2</sub> storage in eddy flux measurements in a forest pertinent to vertical  
931 configurations of a profile system and CO<sub>2</sub> density averaging, *Journal of Geophysical Research*, 112,  
932 10.1029/2006jd008243, 2007.

933 Yang, P. C., Black, T. A., Neumann, H. H., Novak, M. D., and Blanken, P. D.: Spatial and temporal  
934 variability of CO<sub>2</sub> concentration and flux in a boreal aspen forest, *J Geophys Res-Atmos*, 104, 27653-  
935 27661, Doi 10.1029/1999jd900295, 1999.

936 Yao, Y., Zhang, Y., Yu, G., Song, Q., Tan, Z., and Zhao, J.: Estimation of CO<sub>2</sub> storage flux between forest  
937 and atmosphere in a tropical forest, *Journal of Beijing Forestry University*, 33, 23-29, 2011.

938 Zhang, M., Wen, X., Yu, G.-r., Zhang, L.-m., Fu, Y., Sun, X., and Han, S.-j.: Effects of CO<sub>2</sub> storage flux  
939 on carbon budget of forest ecosystem, *Chinese journal of applied ecology*, 21, 1201-1209, 2010.

940 Zhu, J., Gao, T., Yu, L., Yu, F., Yang, K., Lu, D., Yan, Q., Sun, Y., Liu, L., Xu, S., Zhang, J., Zheng, X.,  
941 Song, L., and Zhou, X.: Functions and Applications of Multi-tower Platform of Qingyuan Forest  
942 Ecosystem Research Station of Chinese Academy of Sciences (Qingyuan Ker Towers), *Bulletin of the*  
943 *Chinese Academy of Sciences*, 36, 351-361, 10.16418/j.issn.1000-3045.20210304002, 2021.